Universal transport in periodically driven systems without long-lived quasiparticles

Iliya Esin,[1] Clemens Kuhlenkamp,[2,3,4] Gil Refael,[1,5] Erez Berg,[6] Mark S. Rudner,[7] and Netanel H. Lindner[8]
[1]*Department of Physics, California Institute of Technology, Pasadena, California 91125, USA*
[2]*Department of Physics, Technical University of Munich, 85748 Garching, Germany*
[3]*Munich Center for Quantum Science and Technology, Schellingstrasse 4, D-80799 München, Germany*
[4]*Institute for Quantum Electronics, ETH Zürich, CH-8093 Zürich, Switzerland*
[5]*Walter Burke Institute for Theoretical Physics, California Institute of Technology, Pasadena, California 91125, USA*
[6]*Department of Condensed Matter Physics, Weizmann Institute of Science, Rehovot 76100, Israel*
[7]*Department of Physics, University of Washington, Seattle, Washington 98195-1560, USA*
[8]*Physics Department, Technion, 3200003 Haifa, Israel*

(Received 8 September 2022; revised 14 August 2023; accepted 24 November 2023; published 25 January 2024)

An intriguing regime of universal charge transport at high entropy density has been proposed for periodically driven interacting one-dimensional systems with Bloch bands separated by a large single-particle band gap. For weak interactions, a simple picture based on well-defined Floquet quasiparticles suggests that the system should host a quasisteady state current that depends only on the populations of the system's Floquet-Bloch bands and their associated quasienergy winding numbers. Here we show that such topological transport persists into the strongly interacting regime where the single-particle lifetime becomes shorter than the drive period. Analytically, we show that the value of the current is insensitive to interaction-induced band renormalizations and lifetime broadening when certain conditions are met by the system's nonequilibrium distribution function. We show that these conditions correspond to a quasisteady state. We support these predictions through numerical simulation of a system of strongly interacting fermions in a periodically modulated chain of Sachdev-Ye-Kitaev dots. Our paper establishes universal transport at high entropy density as a robust far from equilibrium topological phenomenon, which can be readily realized with cold atoms in optical lattices.

DOI: 10.1103/PhysRevResearch.6.013094

I. INTRODUCTION

The interplay of topology and far from equilibrium dynamics became an important arena of research in recent years [1–35]. In equilibrium, the field of topology has substantially influenced the modern understanding of electronic systems, contributing to the introduction of fundamental concepts such as topological robustness of quantum states, topological degeneracies of ground states, and non-Abelian anyonic statistics [36–47]. Extension of these concepts to nonequilibrium systems provides the means for dynamical control of topological properties and design of topological phases "on demand" [48–57]. Recently, periodic drives were employed to induce exotic phases of matter without equilibrium analogs [58–69].

An important paradigmatic model of an intrinsically nonequilibrium topological system is the topological pump. The topological pump, originally introduced by Thouless [70], describes a one-dimensional atomic chain with an adiabatically slowly and periodically in time modulated potential. Such a system when tuned to its topological phase supports a robust quantized transport [71–79]. The precise quantization and robustness of adiabatic pumps to external perturbations make them important candidates for applications in quantum metrology [80–84] and processing of quantum information [85–87]. Adiabatic pumps were recently experimentally realized in photonic systems and cold atoms [88–97].

The realization of topological pumps in metallic interacting systems is challenging due to an interplay of interparticle interactions and the nonadiabatic evolution stimulated by the periodic drive. Such an interplay often results in an extensive generation of entropy and incessant heating up of the system to a featureless, high-entropy state [98–100]. The heating can be significantly slowed down in the high driving frequency regime or under special conditions, giving rise to a long-lived prethermal state [101–113]. Recently it was shown that a slowly driven topological pump in the weakly interacting limit can form a quasisteady state [114–116]. In this limit, the quasisteady state can be understood heuristically on the level of free dynamics and weak scattering of particles in well-defined Floquet-Bloch bands. Notably, the quasisteady state hosts a universal current that depends only on the populations of the system's Floquet-Bloch bands and their associated quasienergy winding numbers.

Here we show that the quasisteady state persists into the strongly interacting regime where the single-particle scattering lifetime is shorter than the drive period. Furthermore, in this regime, the current exhibits a similar universal value as in the weakly interacting case, despite the absence of long-lived single-particle Floquet states.

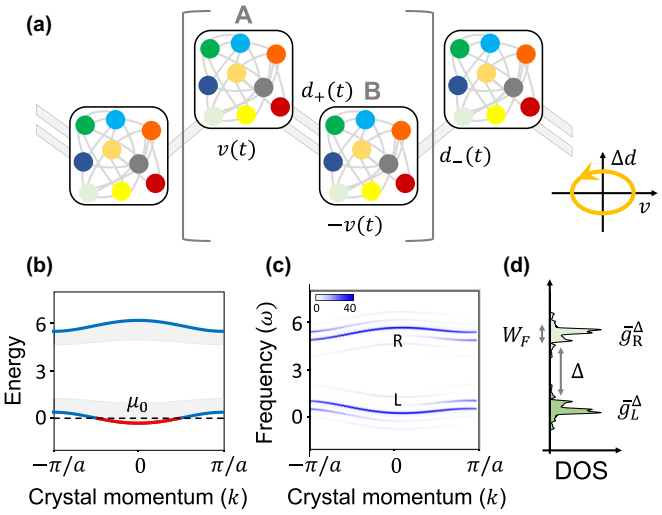

FIG. 1. The model and the single-particle spectrum. (a) Illustration of the system. A chain of atoms with time-modulated hopping and staggered potential, following the driving protocol realizing an adiabatic pump, as shown in the right bottom corner of panel (a) [we denote $\Delta d(t) = d_+(0,t) - d_-(0,t)$]. In the numerical simulation, each site is an SYK dot with $N \to \infty$ orbitals that interact through random interactions [see Eq. (2)]. (b) The single-particle spectrum of the system at $t < 0$, before the drive is switched on. The dashed line represents the Fermi level and the colored section represents initially occupied states, constituting a quarter of all the states in the system. The shaded gray areas show the instantaneous levels of the driven system in one period. The band structure is calculated for $J_0 = 1$, $J_1 = 0.85$, $v_0 = 2.55$, and $\Omega = 0.5$ [see Eq. (1) for the definition of the single-particle Hamiltonian]. (c) The period averaged spectral function of the noninteracting system, $\bar{g}^{\Delta}(k;\omega)$. The labels "L" and "R" indicate the left-movers and the right-movers bands correspondingly. Energy and frequency in panels (b) and (c) are plotted in units of $J_0 = 1$. (d) The period-averaged noninteracting density of states (DOS).

In order to establish the universality of the quasisteady state and demonstrate its emergence across a wide range of interacting models, we studied two models: a topological pump featuring generic short-ranged interactions, and a time-modulated chain of Sachdev-Ye-Kitaev (SYK) dots [117–122] [see Fig. 1(a)]. Despite the contrasting features of these models, we show that they both result in quasisteady states that possess common universal properties. The model with generic short-ranged interactions was employed to provide an analytical account of the quasisteady state and to prove that the current, normalized by the particle density, is quantized in this state.

The time-modulated chain of SYK dots is used to provide numerical evidence of the quasisteady state in a system of strongly interacting fermions with SYK interactions. Our paper demonstrates an approach for numerically exact simulations of driven, strongly interacting chains of many sites, by specializing in SYK-type interactions. This approach is closely related to recent studies of quench dynamics of SYK dots [123–128]. Furthermore, it provides generalization of topological SYK constructions [129,130] into the nonequilibrium topological regime. Our method outperforms the conventional exact diagonalization methods that can be applied to significantly smaller systems. In turn, approximate methods such as Hilbert space decimation (i.e., the time-dependent density matrix renormalization group [131,132]) cannot be applied here, because thermalization dynamics generates long-ranged correlations.

II. DEFINITION OF THE PROBLEM

In this paper, we consider a one-dimensional bipartite chain of L unit cells with periodic boundary conditions, hosting N flavors of otherwise spinless fermions [see Fig. 1(a)]. We label the two sublattices by A and B, and denote the lattice constant by a. For simplicity of notation, throughout we set $\hbar = k_B = e = 1$.

At times $t \geqslant 0$, the evolution of the system is described by the time-periodic Hamiltonian $\hat{\mathcal{H}}(t) = \sum_{k\alpha} \hat{\boldsymbol{c}}^{\dagger}_{k\alpha} H_0(k,t) \hat{\boldsymbol{c}}_{k\alpha} + \hat{\mathcal{H}}_{\rm int}$, where $H_0(k,t)$ denotes the time-periodic single-particle Bloch Hamiltonian and $\hat{\mathcal{H}}_{\rm int}$ denotes the electron-electron interactions. Here, $\hat{\boldsymbol{c}}^{\dagger}_{k\alpha} = (\hat{c}^{\dagger}_{A,k\alpha}, \hat{c}^{\dagger}_{B,k\alpha})$; $\hat{c}^{\dagger}_{s,k\alpha} = \frac{1}{\sqrt{L}} \sum_{j \in j_s} e^{ikaj/2} \hat{c}^{\dagger}_{j\alpha}$, where $\hat{c}^{\dagger}_{j\alpha}$ creates a fermion at a position j with flavor index α; j_s includes all the odd (even) sites for $s = A(B)$. The single-particle Hamiltonian describes the Rice-Mele model [133] with time-periodically modulated parameters:

$$H_0(k,t) = \begin{pmatrix} v(t) - \mu_0 & d(k,t) \\ d^*(k,t) & -v(t) - \mu_0 \end{pmatrix}. \tag{1}$$

Here, $d(k,t) = d_+(k,t) + d_-(k,t)$ and $d_{\pm}(k,t) = e^{\mp ika/2}[J_0 \pm J_1 \sin(\Omega t)]$ and $v(t) = v_0 \cos(\Omega t)$, where $\Omega = 2\pi/T$ is the driving frequency and v_0, J_0, and J_1 are constants. The chemical potential μ_0 sets the average density of the fermions in the chain [see Fig. 1(b)]. For $t < 0$, the system is assumed to be in an equilibrium state with respect to the Hamiltonian $\hat{\mathcal{H}}(t = 0)$, at inverse temperature β_0.

The interparticle interactions are described by the Hamiltonian

$$\hat{\mathcal{H}}_{\rm int} = \sum_{jj'} \sum_{\alpha\beta\gamma\delta} U_{\alpha\beta\gamma\delta}(j,j') \hat{c}^{\dagger}_{j\alpha} \hat{c}_{j\beta} \hat{c}^{\dagger}_{j'\gamma} \hat{c}_{j'\delta} + \text{H.c.} \tag{2}$$

In our analytical study, we assume a single flavor, $\alpha = 1$, and generic short-ranged interactions of characteristic strength $U_{\alpha\beta\gamma\delta}(j,j') = U\chi(|j - j'|)$, where $\chi(|j - j'|)$ is a rapidly decaying dimensionless function of its argument, with $\chi(1) = 1$. (Note that for a single species of fermions, the on-site interaction terms, $j = j'$, do not contribute.) We assume that $\chi(|j - j'|)$ is a short-range function with exponential decay. In the numerical study, we consider the limit of a large number of flavors, N, with $N \to \infty$ [see Fig. 1(a) for an illustration]. Particles of different flavors can locally interact through an SYK-type on-site interaction term, where we consider random and constant in space interactions, $U_{\alpha\beta\gamma\delta}(j,j') = U\chi_{\alpha\beta\gamma\delta}(j,j')$, with $\overline{\chi_{\alpha\beta\gamma\delta}(j,j')} = 0$ and $\overline{\chi^2_{\alpha\beta\gamma\delta}(j,j')} = \delta_{jj'}/N^3$, such that the system preserves invariance to translations for every realization of disordered couplings [121,122]. We expect the model to be self-averaging [134,135], thus providing the same result for any given realization of the random interaction term.

III. NONINTERACTING DYNAMICS

Before studying the interacting model, we briefly summarize the dynamics of the noninteracting topological pump [2,70,77,114,136,137]. We initialize the pump in an equilibrium state of $\mathcal{H}(0)$, at inverse temperature β_0 and a chemical potential μ_0 that fixes the average density of particles at n_0 [see Fig. 1(b)]. The spectral function is initially periodic in k, following the spectrum of the static Hamiltonian, $\mathcal{H}(0)$, as is demonstrated in Fig. 1(b).

After switching on the drive (i.e., for $t > 0$), the dynamics of the system follows the time-dependent Hamiltonian $\mathcal{H}(t)$. Shortly after the quench, the bands of high intensity in the spectral function develop a pronounced structure of sidebands, spaced by the drive frequency Ω, and furthermore obtain nonvanishing net slopes [2] as a function of k [see Fig. 1(c) and attached video [138]]. The peaks of the spectral function at each k correspond to quasienergies associated with the single-particle Floquet state solutions [33,139] of the time-periodic Rice-Mele problem, $[i\partial_t - H_0(k,t)]|\Psi_\nu(k,t)\rangle = 0$, with the multiple values across the different sideband peaks capturing the indeterminacy of quasienergy up to integer multiples of the drive frequency, Ω. The single-particle Floquet states [140,141] are given by $|\Psi_\nu(k,t)\rangle = e^{-i\varepsilon_\nu(k)t}\sum_m e^{-i\Omega m t}|\phi_\nu^m(k)\rangle$, where $\{|\phi_\nu^m(k)\rangle\}$ are time-independent states. Here, $\varepsilon_\nu(k)$ is the corresponding quasienergy of the single-particle state with crystal momentum k, and chirality (or Floquet band) index $\nu = \{\mathrm{L}, \mathrm{R}\}$ for the net left- and right-moving bands, respectively. We denote the bandwidth of the Floquet bands by W_F and the gap between them by Δ. The net chiralities of the bands are determined by the topological index [2,33] $\mathcal{W} = \Omega^{-1}\oint dk\, \partial_k \varepsilon_{R/L}(k) = \pm 1$, where the $+$ $(-)$ sign corresponds to the R (L) band. The chiralities of the bands are exhibited by the spectral function shown in Fig. 1(c). As the momentum changes from $k = -\pi/a$ to $k = \pi/a$, the peaks of the spectral function of the R (L) band shift in frequency from ω to $\omega \pm \Omega$.

IV. TIME EVOLUTION TOWARDS THE QUASISTEADY STATE

We now study the dynamics of the system in the interacting case. In particular, we focus on the evolution of the two-point Green's functions, providing information about expectation values of one-body operators, such as particle densities and the current (see below). The time evolution of the interacting system's two-point Green's functions is described by the Kadanoff-Baym equations [142]

$$[i\partial_t - H_0(t)]G^R(k;t,t') = \delta(t-t') + \Sigma^R \circ G^R, \quad (3a)$$

$$[i\partial_t - H_0(t)]G^<(k;t,t') = \Sigma^R \circ G^< + \Sigma^< \circ G^A, \quad (3b)$$

where for brevity we have suppressed the crystal momentum and time indices on the right hand sides of these equations, and the $\circ$ symbol indicates a convolution over time and matrix product in the sublattice indices. In Eq. (3), the (flavor-averaged) retarded and lesser Green's functions are defined as $G^R_{ss'}(k;t,t') = -\frac{i}{N}\theta(t-t')\sum_{\alpha=1}^N \overline{\langle\{\hat{c}_{s,k\alpha}(t), \hat{c}^\dagger_{s',k\alpha}(t')\}\rangle}_{\rho_0}$, and $G^<_{ss'}(k;t,t') = \frac{i}{N}\sum_{\alpha=1}^N \overline{\langle \hat{c}^\dagger_{s',k\alpha}(t')\hat{c}_{s,k\alpha}(t)\rangle}_{\rho_0}$, while $G^A_{ss'}(k;t,t') = G^R_{s's}(k;t',t)^\dagger$. In these expressions, the expectation values are calculated with respect to the initial state described by the density matrix ρ_0, describing an equilibrium state with respect to $\mathcal{H}(0)$ with temperature β_0 and average density of particles n_0. The bar denotes averaging over the random interaction strength (in the case of the SYK interactions), "{, }" denotes an anticommutator, and $\theta(t)$ is the Heaviside step function. Throughout, we omit the sublattice indices s, s', leaving the 2×2 matrix structure of the Green's functions implicit. The retarded and lesser components of self-energy are denoted by $\Sigma^R(k;t,t')$ and $\Sigma^<(k;t,t')$, respectively [see Fig. 2(a) and Appendix C for technical details].

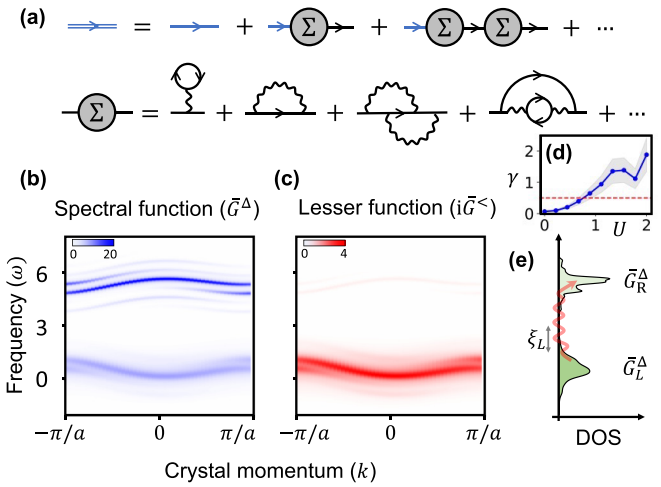

FIG. 2. Renormalization of the spectrum by interactions. (a) First row: Dyson's expansion for the band resolved Green's function. The double and single blue lines indicate the band-resolved renormalized and bare functions respectively. Black lines denote the full bare Green's function. Second row: Diagrammatic expansion of the self-energy, used in the analytical model (shown up to order U^2). In the numerics, we considered SYK interactions in the infinite N limit, in which all the diagrams with an odd number of interaction vertices or with crossed lines are averaged to zero [i.e., only the last diagram in (a) contributes]. (b) Period-averaged trace of the spectral function, $\bar{G}^\Delta(k;\omega) = \sum_s \frac{1}{T}\int_0^T d\bar{t} G^\Delta_{ss}(k;\omega,\bar{t})$, renormalized by the SYK interactions with $U = 1$. (c) Period-averaged trace of the lesser function, $\bar{G}^<(k;\omega) = \sum_s \frac{1}{T}\int_0^T d\bar{t} G^<_{ss}(k;\omega,\bar{t})$, indicating occupation after 30 periods of the drive, for the same parameters as in (b). Note the weak, yet finite occupation of the upper band produced by the interband processes. (d) Inverse lifetime of the quasiparticles, γ, extracted from the spectral function width, as a function of U. The dashed line denotes the driving frequency, Ω. (e) The renormalized period-averaged single-particle DOS. In the presence of interaction, the noninteracting DOS appearing in Fig. 1(d) broadens, obtaining exponential tails ξ_ν. The broadening creates an overlap between the upper and lower bands, forming an interband heating channel (indicated by the wiggly arrow). Frequencies are plotted in units of $J_0 = 1$.

A. Single-particle spectral function

The renormalized single-particle spectrum of the nonequilibrium system is encoded in the retarded Green's function, whose time evolution is given by Eq. (3a). In order to facilitate the separation of intraband and interband scattering processes below, we write the full retarded Green's function as a sum of

R- and L-band projected Green's functions: $G^R = G^R_R + G^R_L$. The band-resolved Green's functions are defined through the Dyson series shown in Fig. 2(a), corresponding to Dyson's equation,

$$G^R_\nu(k;t,t') = g^R_\nu(k;t,t') + g^R_\nu \circ \Sigma^R \circ G^R, \tag{4}$$

where, as in Eqs. (3a) and (3b), we suppress the crystal momentum and time indices on the last term for brevity. Here, $g^R_\nu(k;t,t')$ is the noninteracting retarded Green's function projected to band ν (see Appendix A for more details).

We define the renormalized band-resolved spectral functions as $G^\Delta_\nu(k;\omega,\bar{t}) = i[G^R_\nu(k;\omega,\bar{t}) - G^A_\nu(k;\omega,\bar{t})]$, where $G^R_\nu(k;\omega,\bar{t})$ is obtained via the Wigner transform of the two-time function, $G^R_\nu(k;t,t')$, with $\bar{t} = \frac{1}{2}(t+t')$, and $G^A_\nu(k;\omega,\bar{t}) = [G^R_\nu(k;\omega,\bar{t})]^\dagger$. The renormalized band-resolved spectral functions exhibit the same chiralities as the bare ones, as can be observed from the frequency shifts of the peaks of $\bar{G}^\Delta(k;\omega)$ from ω to $\omega \pm \Omega$ as k changes from $-\pi/a$ to π/a [compare Figs. 1(c) and 2(b)]. With interactions, the peaks of the spectral function become broad, with tails extending into the gap while decaying approximately as $e^{-\omega/\xi_\nu}$.

The renormalization of the single-particle spectral function is caused by the dressing of the noninteracting Floquet bands by virtual electron-hole pair creation and annihilation processes. Our analytical estimate near the quasisteady state (see Appendix C) suggests that the broadening of G^Δ_L in the limit $W_F \ll U \ll \Delta$ is approximately given by $\xi_L \approx -W_F/\ln(\frac{U^2}{\Delta^2}[f^0_L\bar{f}^0_L + f^0_R\bar{f}^0_R])$, where f^0_L and f^0_R are the occupation probabilities of the Floquet bands (see below) and $\bar{f}^0_\nu = 1 - f^0_\nu$.

Furthermore, the width of G^Δ_L is associated with the lifetime of the quasiparticles. Figure 2(d) demonstrates the inverse quasiparticle lifetime, γ, extracted at $k = 0$ (γ is approximately uniform in k), as a function of U, with the red dashed line indicating the driving frequency, Ω. Remarkably, near $U = 1$, the quasiparticle lifetime becomes shorter than the period of the drive. This is an intriguing regime in which the Floquet states and the associated Floquet spectrum cannot be resolved. In what follows, we are particularly interested in the quasisteady state in this regime, where naïvely, the topological pumping should not persist.

B. The kinetic equation and population dynamics

To study the formation and properties of the quasisteady state, we define occupation probabilities by parametrizing the lesser Green's function as

$$G^<(k;t,t') = f_R \circ G^A_R - G^R_R \circ f_R + f_L \circ G^A_L - G^R_L \circ f_L, \tag{5}$$

where crystal momentum and time indices are suppressed on the right hand side. By analogy to the case of thermodynamic equilibrium, where the (Fourier-transformed) lesser Green's function and the spectral function are related via the Fermi occupation function, in Eq. (5) the Hermitian matrices $f_R(k;t,t')$ and $f_L(k;t,t')$ play the roles of distribution functions for the two bands. As we will discuss further below, this interpretation is most meaningful when $f_R(k;t,t')$ and $f_L(k;t,t')$ take simple forms in terms of their matrix and time (or frequency) structures. We will see that such a simple form naturally emerges in the quasisteady state of the system.

To assess the dynamics of the distribution functions we derive a kinetic equation for $\partial_{\bar{t}} f_L(k;\omega,\bar{t})$, where $f_L(k;\omega,\bar{t})$ is obtained via the Wigner transform of the two-time function, $f_L(k;t,t')$. A similar approach is often employed in studies of dynamical systems [143–145] using an "on-shell" approximation. Such an approximation would not correctly capture interband scattering, which occurs through high-order processes in U. To capture these processes we derive the kinetic equation for f_ν without imposing the on-shell approximation [146].

The kinetic equation is obtained by combining the Wigner transforms of Eqs. (5) and (3b) and subtracting terms proportional to $\partial_{\bar{t}} G^R(k;\omega,\bar{t})$, which itself is described by Eq. (3a) (see Appendix D for the full derivation). Generically, the kinetic equation for f_L can be written as [147] $\partial_{\bar{t}} f_L(k;\omega,\bar{t}) = \mathcal{I}_L(k;\omega,\bar{t})\{f_R, f_L\}$, where the collision integral $\mathcal{I}_L$ is a functional of f_R and f_L with a matrix structure in the sublattice indices. Notably, for values of ω where $G^\Delta_L(k;\omega,t)$ has significant weight, i.e., near the lower band [see Fig. 2(d)], the net collision integral is exponentially small if its arguments are independent of k and ω (see Appendix D): $f^{(\mathrm{qs})}_L(k;\omega,\bar{t}) = f^0_L\mathbf{1}$, $f^{(\mathrm{qs})}_R(k;\omega,\bar{t}) = f^0_R\mathbf{1}$, where f^0_L and f^0_R are constants and $\mathbf{1}$ denotes the identity matrix in sublattice space. In particular, we estimate $\mathcal{I}_L\{f^{(\mathrm{qs})}_L, f^{(\mathrm{qs})}_R\} \propto e^{-\Delta/\xi}\delta f$, where $\delta f = f^0_R - f^0_L$. A state described by this form of $f^{(\mathrm{qs})}_\nu$, characterized by uniform occupation within each band, exhibits exponentially slow population dynamics and thus describes a long-lived quasisteady state of the system.

Therefore, following Eq. (5) and the expressions for $f^{(\mathrm{qs})}_{L/R}(k;\omega,\bar{t})$, the lesser function in the quasisteady state reads

$$G^<_{(\mathrm{qs})}(k;\omega,\bar{t}) = f^0_R G^\Delta_R(k;\omega,\bar{t}) + f^0_L G^\Delta_L(k;\omega,\bar{t}) + \mathcal{O}(e^{-\Delta/\xi}). \tag{6}$$

This relation between the lesser function and the chirality-projected spectral functions in the quasisteady state is manifested in Figs. 2(b) and 2(c). Comparing these two figures, we see that the lower band of $G^<$ is proportional to the lower band of G^Δ and the upper band of $G^<$ is proportional to the upper band of G^Δ, with the proportionality constants $f^0_L \approx an_0$, and $f^0_R \approx 0$.

C. Universal value of the current

Using the form of the quasisteady state found above in terms of two-point Green's functions, we can now characterize *observables* in the quasisteady state. In particular we focus on the value of the time-averaged current, which was previously conjectured to take a universal value based on a weak-coupling picture and evidence from numerical simulations on modestly sized systems.

The instantaneous current averaged along the chain in a generic translation-invariant state described by $G^<$ reads

$$\mathcal{J}(t) = -i\int \frac{dk}{2\pi}\mathrm{Tr}\{G^<(k;t,t+0^+)\partial_k H_0(k,t)\}, \tag{7}$$

where the momentum integral is performed over the first Brillouin zone. Next, we evaluate Eq. (7) in the quasisteady state given by Eq. (6). At equal times, $G^<_{(\mathrm{qs})}$ can be

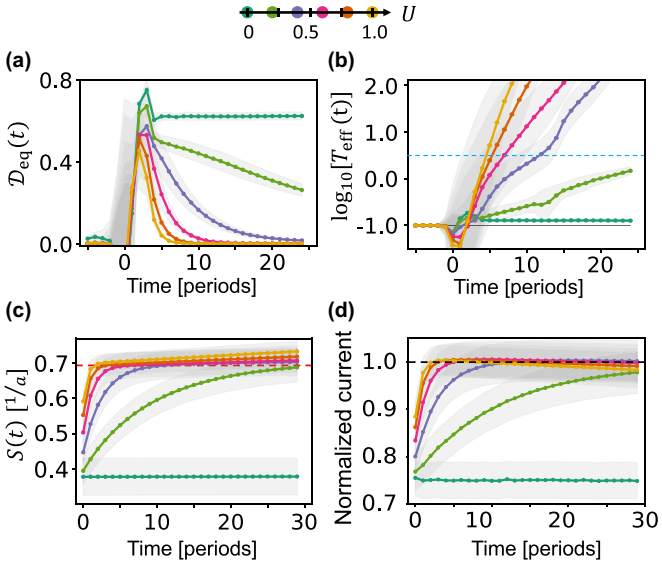

FIG. 3. Relaxation to the quasisteady state. (a) "Distance" to equilibrium, $\mathcal{D}_{\rm eq}(t)$, defined in Eq. (8), as a function of time. Lines of different colors in this and following panels correspond to the different interaction strengths indicated on the top of the figure, in units of $J_0 = 1$. Shaded areas indicate error bars due to the extrapolation procedure; see text. At $t = 0$, the extrapolation yields nonphysical, negative values of $\mathcal{D}_{\rm eq}(t)$ due to the quench; we thus cut off these values in the plot. (b) Effective temperature of the lower band minimizing $\mathcal{D}_{\rm eq}(t)$ in units of $J_0 = 1$, as a function of time. The blue dashed line indicates the point where $\mathcal{T}_{\rm eff} = W_{\rm F}$. (c) Entropy density of the system's one-body reduced density matrix as a function of time, defined in Eq. (9). A dashed line indicates maximal entropy for a quarter-filled system, when all the particles occupy the lower band. (d) Period averaged current normalized by the total density of particles and driving frequency, $\bar{\mathcal{J}}(t)(T/\nu_0)$ as a function of time.

further simplified using $G^{\Delta}_{\nu}(k;t,t+0^+) = g^{\Delta}_{\nu}(k;t,t+0^+)$. The latter identity directly follows from Eq. (4), because the time-convolution integrals in the right hand side of Eq. (4) vanish for $t' \to t$. In the frequency domain this identity reads $\int d\omega G^{\Delta}_{\nu}(k;\omega,\bar{t}) = \int d\omega g^{\Delta}_{\nu}(k;\omega,\bar{t})$, yielding conservation of the total spectral weight in each chirality.

Substituting the resulting quasisteady state form of $G^{<}_{\rm (qs)}$ into Eq. (7), we obtain $\mathcal{J}(t) = f^0_R \mathcal{J}^0_R(t) + f^0_L \mathcal{J}^0_L(t)$, where $\mathcal{J}^0_\nu = \int \frac{dk}{2\pi} \langle \Psi_\nu | \partial_k H_0 | \Psi_\nu \rangle$ is the current carried by Floquet band ν of the system in the absence of interactions, when fully filled (see Appendix A). As defined in Sec. III above, $|\Psi_\nu(k,t)\rangle$ denotes the single-particle Floquet state with crystal momentum k in band ν of the system in the absence of interactions. In the adiabatic limit, the period averaged current $\bar{\mathcal{J}}^0_\nu = \frac{1}{T}\int_0^T dt \mathcal{J}^0_\nu$ is quantized [70] as $\bar{\mathcal{J}}^0_{R,L} = \pm\frac{1}{T}$. In a system where the upper (R) band is initially empty and the lower (L) band has fractional filling $\nu_0 = an_0$, we therefore expect $f^0_L = \nu_0$ and $f^0_R = 0$, such that the current in the quasisteady state is equal to $\bar{\mathcal{J}}^{\rm (qs)} = \frac{\nu_0}{T} + \mathcal{O}(e^{-\Delta/\xi})$, where the correction captures the deviation of the quasisteady state from the maximal entropy state in which the upper band is empty. Figure 3(d) demonstrates the quantization of the current normalized by ν_0 in the quasisteady state obtained in the numerical simulation (see the details below).

This is a remarkable result: even in a limit where the single-particle scattering lifetime may be short compared with the driving period [see Fig. 2(d)], where the single-particle Floquet states and associated spectrum are not well resolved or defined, the current still attains a universal value associated with the nontrivial topology of the system's single-particle Floquet spectrum in the absence of interactions. The universal value of current holds, up to an exponentially small correction, provided that the scattering rate (and associated level broadening, captured by ξ) remains small compared with the single-particle band gap, Δ.

V. NUMERICAL ANALYSIS

To provide extra support of the quasisteady state and demonstrate its pertinence in a class of interacting models, we numerically simulated the model given in Eqs. (1) and (2), with SYK interactions. The SYK-type interactions provide exact solutions in the large-N limit. We note that the unique critical properties of the SYK model [119] are not important here, because the single-particle gap, Δ, is the dominant scale. In addition to the terms described above, we also included a weak random quadratic term $\hat{\mathcal{H}}_{\rm SYK-2} = \sum_{j,\alpha\beta} K_{\alpha\beta}\hat{c}^\dagger_{j\alpha}\hat{c}_{j\beta} +$ H.c., where $\overline{K_{\alpha\beta}} = 0$ and $\overline{K^2_{\alpha\beta}} = K^2/N$, with $K = 0.05$. This additional term is essential for stabilizing the numerics in the weakly interacting regime. We set the value of K to about 1% of Δ, ensuring its impact on the dynamics is negligible.

The unique structure of the SYK interactions allows us to simulate considerably larger systems compared to exact diagonalization methods applied to systems with conventional interactions. Here, we simulated the time evolution of a chain of 100 SYK dots arranged into $L = 50$ unit cells. We used the Kadanoff-Baym equations [given in Eq. (3)] to evolve the Keldysh-ordered Green's functions in time [112,123–128,148,149]; for further details see Appendix E. The system is initialized in an equilibrium state of $\hat{\mathcal{H}}(0)$ with temperature $\beta_0^{-1} = 0.1$ and $\mu_0 = -2.93$, which is set to fix the density of electrons approximately at quarter filling [see Fig. 1(b)]. For the model itself, we select the parameter values: $J_0 = 1$, $J_1 = 0.85$, $v_0 = 2.55$, $\Omega = 0.5$ [see Eq. (1) and surrounding text for the definitions of the Hamiltonian and its parameters]. We note that all the energies and frequencies are given in units in which $J_0 = 1$.

The time-evolution algorithm is based on the discretization of the time and frequency domains, with small steps δt and $\delta\omega$, respectively. We performed the evolution for several values of steps in the range $0.08 \leqslant \delta t \leqslant 0.16$ and $0.015 \leqslant \delta\omega \leqslant 0.04$, and performed a two-dimensional linear extrapolation to $\delta t = \delta\omega = 0$. In the numerical results we present the extrapolated values with error bars indicating the uncertainty of the extrapolation procedure (defined as the difference between the extrapolated value and the closest numerically determined point).

A. Formation of the quasisteady state

We first analyze the formation of the quasisteady state, wherein the distribution functions f_L and f_R for the two

bands become independent of crystal momentum and frequency, while the total populations of the two bands remain approximately constant. As a means of characterizing the nonequilibrium state of the system, and to enable the extraction of an effective temperature (when it is appropriate to do so), we define the "distance" of the distribution from a thermal equilibrium state as

$$\mathcal{D}_{\rm eq}(\bar{t}) = \min_{\beta,\mu} \int \frac{adk}{2\pi} \int_{-\infty}^{\omega_c} \frac{d\omega}{2\pi} {\rm Tr}|i\overline{G}^{<} + f_{\rm FD}(\beta,\mu)\overline{G}^{\Delta}|, \quad (8)$$

where ω_c is the center of the spectrum and the Green's functions are evaluated in the Wigner transformed representation and averaged over one period: $\overline{G}^{<}(k;\omega,\bar{t}) \equiv \frac{1}{T}\int_{-T/2}^{T/2} ds\, G^{<}(k;\omega,\bar{t}+s)$ and similarly for $\overline{G}^{\Delta}(k;\omega,\bar{t})$. Here, $f_{\rm FD}(\beta,\mu) = [1+e^{\beta(\omega-\mu)}]^{-1}$ is the Fermi function. For a system in thermal equilibrium, the integrand in Eq. (8) vanishes for all k and ω, corresponding to $\mathcal{D}_{\rm eq} = 0$.

In Figs. 3(a) and 3(b) we plot the evolution of the distance to equilibrium $\mathcal{D}_{\rm eq}(\bar{t})$ and the extracted effective temperature $\mathcal{T}_{\rm eff} = \beta_{\rm min}^{-1}$, corresponding to the minimization in Eq. (8). When the drive is quenched at $\bar{t} = 0$, $\mathcal{D}_{\rm eq}$ rapidly grows, indicating evolution into a far from equilibrium state. We should note that $\mathcal{D}_{\rm eq}$ exhibits a small signal even at $\bar{t} < 0$, which arises because $\mathcal{D}_{\rm eq}$ is defined from Wigner functions that possess uncertainty in $\bar{t}$. During the quench, the system undergoes a highly nonequilibrium evolution. As a result, the expectation values become unstable, which is manifested by large error bars (indicated by shaded areas in Fig. 3).

Following the quench, the "distance to equilibrium" rapidly increases, indicating the formation of a nonequilibrium state, because the population after the quench is not diagonal in the Floquet basis. However, it is important to note that the momentum distribution of the population immediately after the quench is the same as the prequench distribution, leading to only a slight change in $\mathcal{T}_{\rm eff}$ [150]. Following the rapid increase, $\mathcal{D}_{\rm eq}$ decays to zero as the system relaxes to a quasisteady state. Simultaneously, the effective temperature grows approximately exponentially with a rate $\Gamma_{\rm intra}$: $\mathcal{T}_{\rm eff} \sim \beta_0^{-1} e^{\Gamma_{\rm intra} t}$ [Fig. 3(b)]. Importantly, at short times after the quench, the fluctuation-dissipation theorem is not applicable, as indicated by a large $\mathcal{D}_{\rm eq}$. Consequently, $\mathcal{T}_{\rm eff}$ is ill defined in this regime, giving rise to large error bars near $t = 0$.

The quasisteady state observed in the simulation approximately realizes the conditions discussed in Sec. IV B, once the effective temperature exceeds the width of the single-particle Floquet bands, $\mathcal{T}_{\rm eff} \gg W_{\rm F}$, indicated by blue dashed line (and for $\mathcal{D}_{\rm eq} \ll 1$). The curves of different colors in Figs. 3(a) and 3(b) correspond to different interaction strengths, U; the time to reach the quasisteady state rapidly decreases with interaction strength, U.

To track the system's evolution towards a high entropy density state, we calculated the average von Neumann entropy density of the system's one-body reduced density matrix:

$$S(\bar{t}) = -{\rm Tr}\int \frac{dk}{2\pi}[(-i\overline{G}^{<})\log(-i\overline{G}^{<}) + (i\overline{G}^{>})\log(i\overline{G}^{>})], \quad (9)$$

where $\bar{G}^{>} = -i\bar{G}^{\Delta} + \bar{G}^{<}$ and the Green's functions are evaluated at equal times $t = t' = \bar{t}$ [see Fig. 3(c)]. The value of $S(\bar{t})$ for a maximal entropy density state in a quarter-filled system, subject to the constraint that all the particles occupy the lower band, is given by $S_L^{\rm max} = \log(2)/a$. As can be seen in Fig. 3(c), the entropy density stabilizes slightly above this value due to a small population excited to the upper band at $t = 0$. After stabilizing near $S(t) \approx S_L^{\rm max}$, the entropy slowly grows further due to interband transitions. In the infinite time limit, we expect $S \to S^{\rm max} \approx 1.12/a$ corresponding to one-quarter filling of the entire system.

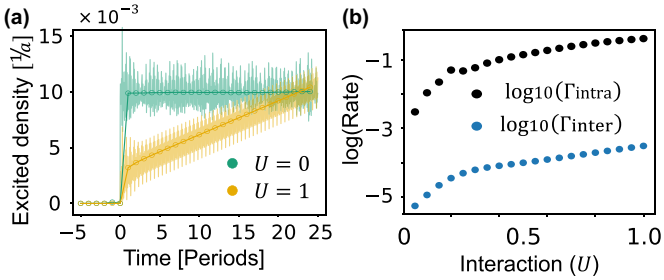

FIG. 4. Heating and current in the quasisteady state. (a) Density of electrons excited to the upper band as a function of time, in the interacting and noninteracting cases. Circles represent the period averaged density. In the interacting case, the density of excitations increases with an approximately constant rate $\Gamma_{\rm inter}$, while in the noninteracting case the average charge is constant, following an initial jump at $t = 0$. (b) Intraband ($\Gamma_{\rm intra}$) and interband ($\Gamma_{\rm inter}$) equilibration rates as a function of the interaction strength. The intraband equilibration rate is extracted from the temperature growth [see Fig. 3(b)]. The interband equilibration rate is extracted from the slope of the period-averaged excitation density, in (a).

In Fig. 3(d), we extracted the period-averaged current normalized by the filling, $\bar{\mathcal{J}}/\nu_0$ [see Eq. (7)]. As follows from the discussion below Eq. (7), we expect an approximately quantized value in the units of T^{-1} for the normalized current in the quasisteady state. Figure 4(b) shows the period-averaged current normalized by ν_0 as a function of the stroboscopic time. The gray strips indicate the uncertainty intervals associated with the extrapolation to infinitesimal grid spacing in the simulations, as described above. In the regime of strong interactions, the average current rapidly increases on a timescale set by $\sim\Gamma_{\rm intra}$. When the quasisteady state is reached, the current obtains the expected universal value to within the uncertainties of the numerical simulation, as expected. For later times, the current slowly decays with the rate $\Gamma_{\rm inter}$ due to interband heating. In the weakly interacting case, the normalized current remains nonuniversal for much longer times; for these cases, the quasisteady state was not reached within the time window that we were able to simulate. Interestingly, slowly driven Fermi liquids have been shown to persist in nonthermal states for parametrically long timescales [112]. The connection between the slow intraband heating observed here and the mechanism in Ref. [112] will be interesting to investigate in future work.

B. Interband heating and universal current

To investigate the interband scattering processes and measure their rates, in Fig. 4(a) we extracted the density of excitations in the (renormalized) R band from our

simulations. We define the excitation density as $n_{\rm ex}(\bar{t}) = -i\int_{\omega_c}^{\infty}\frac{d\omega}{2\pi}\int\frac{dk}{2\pi}{\rm Tr}\{G^<(k;\omega,\bar{t})\}$. The period-averaged density of excitations jumps at $\bar{t}=0$, when the drive is switched on [137], and then gradually increases with an approximately constant rate $\Gamma_{\rm inter}$. The interband equilibration rate, $\Gamma_{\rm inter}$, compared to the intraband equilibration rate, $\Gamma_{\rm intra}$, is shown as a function of the interaction strength in Fig. 4(b).

Figure 2(c) shows the period averaged lesser Green's function as a function of momentum and frequency, after 30 periods of the drive. The excited population can be seen as a pale strip at the location of the upper band. Note that the features are heavily broadened due to fast intraband scattering, such that for the selected parameters the Floquet harmonic sidebands are nearly completely washed out.

VI. DISCUSSION AND OUTLOOK

Periodically driven systems can host Floquet-Bloch bands with unique topological properties that cannot be obtained in equilibrium systems. In the presence of interactions, it is natural to wonder if rapid scattering on timescales comparable to the driving period might mask any dynamical features expected to arise from the single-particle Floquet states. In this paper we showed that this need not be the case: even in a state with high entropy density and rapid scattering, universal transport associated with the topological properties of the system's Floquet Bloch bands persists, when the instantaneous gap is the dominant energy scale in the problem. We demonstrated this phenomenon in the context of a topological pump with noninteger filling, which exhibits a long-lived quasisteady state with maximal entropy density (subject to the constraint of fixed particle number in each band). We derived conditions under which the quasisteady state hosts quantized transport (in units of the particle density), up to an exponentially small correction in the ratio of the system's band gap to its renormalized bandwidth.

To support these arguments, we studied this phenomenon numerically in an SYK-type chain. This setup enabled us to examine the dynamics in a regime of strong scattering, in system sizes much larger than could be accessed by exact evolution. This advantage is gained from the fact that the SYK system can be solved by time evolution of the Kadanoff-Baym equations. Our numerical results allowed us to study the dynamics leading to the formation of the quasisteady state. Importantly, we showed that quantized transport persists even when quasiparticles are short lived due to fast intraband scattering and the Floquet sidebands are hence not well resolved.

ACKNOWLEDGMENTS

We would like to thank Ervand Kandelaki and Michael Knap for illuminating discussions, and David Cohen and Yan Katz for technical support. N.H.L. acknowledges support from the European Research Council (ERC) under the European Union Horizon 2020 Research and Innovation Programme (Grant No. 639172), and from the Israeli Center of Research Excellence (I-CORE) "Circle of Light." M.S.R. gratefully acknowledges the support of the ERC under the European Union Horizon 2020 Research and Innovation Programme (Grant No. 678862) and the Villum Foundation. M.S.R. and E.B. acknowledge support from CRC 183 of the Deutsche Forschungsgemeinschaft. G.R. acknowledges support from the U.S. Department of Energy, Office of Science, Basic Energy Sciences under (Grant No. desc0019166) and the Simons Foundation. I.E. is grateful for support from the Simons Foundation and the Institute of Quantum Information and Matter.

APPENDIX A: THE BAND-RESOLVED BARE GREEN'S FUNCTION

Here, we present the derivation of the retarded band-resolved bare Green's function [see Figs. 1(c) and 1(d)]. In the noninteracting case the flavors [denoted by α in Eq. (2)] are independent of each other. We thus focus on $\alpha=1$ and omit the flavor index. The bare retarded Green's function is defined as

$$g^R_{ss'}(k;t,t') = -i\langle\{\hat{c}_{s,k}(t),\hat{c}^\dagger_{s',k}(t')\}\rangle\theta(t-t'), \tag{A1}$$

where $s,s'=\{A,B\}$ are the sublattice indices, and $\hat{c}_{s,k}(t) = \hat{U}^\dagger(t)\hat{c}_{s,k}(0)\hat{U}(t)$. The unitary evolution operator is given by $\hat{U}(t)=\mathcal{T}e^{-i\int_{-\infty}^{t}\hat{\mathcal{H}}(t')dt'}$, where $\hat{\mathcal{H}}(t)$ is given in Eq. (1). For t and t' well after the quench, the time-dependent Hamiltonian can be diagonalized, by the Floquet eigenstates $|\Psi_\nu(k,t)\rangle$, for $\nu=R,L$. In this eigenbasis the fermionic operators read

$$\hat{c}_{s,k}(t) = \langle s|\Psi_R(k,t)\rangle\hat{d}_{R,k} + \langle s|\Psi_L(k,t)\rangle\hat{d}_{L,k}, \tag{A2}$$

where $\hat{d}_{\nu,k}$ annihilate the Floquet state $|\Psi_\nu(k,t)\rangle$ and $\langle s|\Psi_\nu(k,t)\rangle$ is the amplitude of the Floquet state projected onto a sublattice s. Substituting Eq. (A2) in Eq. (A1), and evaluating $\langle\{\hat{d}^\dagger_{\nu,k},\hat{d}_{\nu',k}\}\rangle=\delta_{\nu\nu'}$, we arrive at

$$\begin{aligned} g^R_{ss'}(k;t,t') = &-i\theta(t-t') \\ &\times[\langle s|\Psi_R(k,t)\rangle\langle\Psi_R(k,t')|s'\rangle \\ &+\langle s|\Psi_L(k,t)\rangle\langle\Psi_L(k,t')|s'\rangle]. \end{aligned} \tag{A3}$$

Following Eq. (A3), we define the right/left chirality Green's functions as

$$g^R_\nu(k;t,t') = -i\theta(t-t')|\Psi_\nu(k,t)\rangle\langle\Psi_\nu(k,t')|. \tag{A4}$$

Note that $g^R_\nu(k;t,t')$ is essentially a projector to one of the Floquet bands and therefore has a matrix structure in the sublattice indices. The original Green's function [defined in Eq. (A1)] is given by the sum of the band-resolved Green's functions, $g^R_{ss'}(k;t,t') = \langle s|g^R_R(k;t,t')+g^R_L(k;t,t')|s'\rangle$.

1. Wigner representation of the retarded Green's function

Next, we derive the Winger-transformed representation of the band-resolved Green's function, given in Eq. (A4). The Wigner transform of $g(k;t,t')$ is defined as

$$g(k;\omega,\bar{t}) = \int e^{i\omega\delta t}g(k;\bar{t}+\delta t/2,\bar{t}-\delta t/2)d\delta t. \tag{A5}$$

To evaluate Eq. (A5), we substitute the harmonic expansion of the Floquet states, $|\Psi_\nu(k,t)\rangle = e^{-i\varepsilon_\nu(k)t}\sum_m e^{-i\Omega mt}|\phi^m_\nu(k)\rangle$ (see Sec. IV) in Eq. (A4). We then perform the δt integral,

yielding [151]

$$g_\nu^R(k;\omega,\bar{t}) = \sum_{m,n} \frac{|\phi_\nu^{m+n}(k)\rangle\langle\phi_\nu^{m-n}(k)|}{\omega - \varepsilon_\nu(k) + m\Omega + i0^+} e^{-2in\Omega\bar{t}}. \quad \text{(A6)}$$

The period averaged Green's function [see Fig. 1(c)] can be extracted from the $n = 0$ terms in Eq. (A6), yielding

$$\bar{g}_\nu^R(k;\omega) = \sum_m \frac{|\phi_\nu^m(k)\rangle\langle\phi_\nu^m(k)|}{\omega - \varepsilon_\nu(k) + m\Omega + i0^+}. \quad \text{(A7)}$$

APPENDIX B: DEFINITION OF THE KELDYSH-FLOQUET GREEN'S FUNCTIONS IN THE GAUGE-INVARIANT FORM

Due to the nonequilibrium nature of the Floquet-Keldysh Green's functions, the energy in the collision processes is only conserved modulo Ω. This property complicates the calculations using the Keldysh formalism, as multiple photon absorption/emission processes have to be taken into account in each collision. Here, we present a gauge invariant definition of the Green's functions in which the ω index is conserved in the collision processes, and show how the convolution and product of the two-time Green's functions are defined with this gauge choice. Such a definition allows us to operate the Keldysh-Floquet Green's functions as equilibrium Keldysh Green's functions with additional matrix structure in the Floquet harmonics.

Given the Wigner-transformed Green's function $G(\omega,\bar{t})$ [see Eq. (A5) for definition], we define the Green's function in the harmonic basis (with indices $m, n \in \mathbb{Z}$) as

$$G_{mn}(\omega) = \frac{1}{T}\int_0^T d\bar{t} G(\omega + \frac{m+n}{2}\Omega, \bar{t}) e^{i\Omega(m-n)\bar{t}}. \quad \text{(B1)}$$

This definition is invariant under the transformation $G_{m,n}(\omega + l\Omega) = G_{m+l,n+l}(\omega)$ for any integer l. A convolution $C(t,t') = \int ds A(t,s)B(s,t)$ reads

$$C_{mn}(\omega) = \sum_l A_{ml}(\omega)B_{ln}(\omega). \quad \text{(B2)}$$

Similarly, a product of two same-time functions, $P(t,t') = A(t,t')B(t,t')$, is given by

$$P_{mn}(\omega) = \sum_l \int \frac{d\omega'}{2\pi} A_{m-l,n}(\omega-\omega')B_{l,0}(\omega'). \quad \text{(B3)}$$

APPENDIX C: EVALUATION OF THE SELF-ENERGY AND RENORMALIZATION OF THE SPECTRAL FUNCTION

Here, we estimate the broadening ξ of the renormalized bandwidth of the Floquet bands in the quasisteady state, discussed in Sec. IV A. In all the expressions in this section, we assume the Green's functions in the frequency domain are defined as matrices in the harmonic basis [as defined in Eq. (B1)], and implicitly contract the harmonic indices following the rules given in Eqs. (B2) and (B3). The renormalization of the spectral width can be understood from the definition of the renormalized Green's function in terms of the bare one:

$$[G^R(\omega)]^{-1} = [g^R(\omega)]^{-1} - \Sigma^R(\omega), \quad \text{(C1)}$$

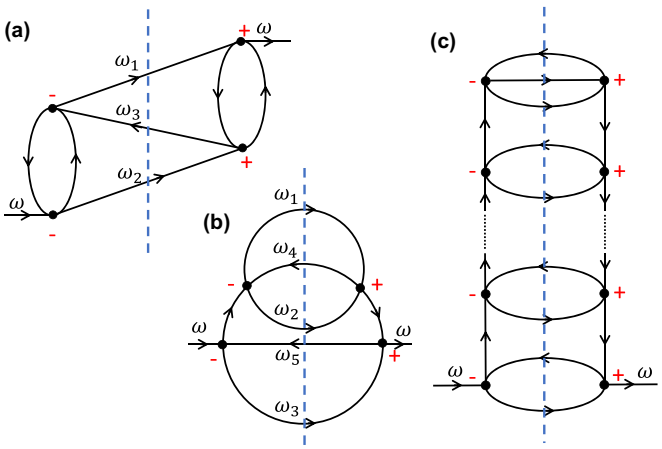

FIG. 5. Examples of diagrams contributing to the self-energy, $\Sigma^>(\omega)$, arranged such that the vertices on the positive Keldysh branch are at the left side and the vertices on the negative Keldysh branch are at the right side. Notice that the left diagram would not contribute in the case of the SYK interactions, since it is subleading in the number of the SYK flavors.

following from Eq. (3a). Focusing on the values of ω at the gap of the bare function, i.e., where $g^\Delta(\omega) = 0$, the renormalized spectral function reads

$$G^\Delta(\omega) \approx -[g^R(\omega)]^2\Sigma^\Delta(\omega). \quad \text{(C2)}$$

Therefore, to estimate the broadening of the spectral function, we need to estimate $\Sigma^\Delta(\omega)$. In what follows, we estimate the momentum-averaged lesser and greater components of the self-energy $\Sigma^{\gtrless}(\omega)$, constituting the spectral component, $\Sigma^\Delta = i\Sigma^> - i\Sigma^<$.

To estimate the self-energy, we need to sum over all irreducible diagrams allowed by the interaction term [the first four terms in the expansion are demonstrated in Fig. 2(a)]. We begin by estimating the greater component of the self-energy, $\Sigma^>(\omega)$. Consider a generic irreducible diagram in this sum, corresponding to the order U^p in the interaction strength (see Fig. 5). Such a diagram contains p interaction vertices evaluated at the times t_1, $t_2, \ldots, t_p$ and positions on the Keldysh contour $i_1, \ldots, i_p$, where $i_p = \pm$ corresponding to positive (+) and negative (−) branches on the Keldysh contour. The vertices are connected by the noninteracting propagators $g_{i,i'}(t,t')$, with the convention $g_{+-} = g^<$, $g_{-+} = g^>$, $g_{++} = g^T$, and $g_{--} = g^{\tilde{T}}$. For a specific combination of i_p, it is useful to arrange the diagram such that all the vertices on the positive branch are on the left side and all the vertices on the negative branch are on the right side (see Fig. 5). Notice that by the definition of $\Sigma^>$ the incoming vertex belongs to the negative Keldysh branch and the outgoing vertex belongs to the positive branch.

Next, we transform the expression for the self-energy following the transformation given in Eq. (B1). For convenience, we enumerate the frequencies of the l propagators going from the left to the right side of the diagram by $\omega_1, \omega_2, \ldots, \omega_l$, and $l-1$ propagators going from the right side to the left side by $\omega_{l+1}, \omega_{l+2}, \ldots, \omega_{2l-1}$, for $l \geqslant 1$. The maximal value of l is limited by p. We define the sum of the frequencies of the

propagators crossing the center of the diagram with opposite signs by $\Delta\omega = \omega_1 + ... + \omega_l - \omega_{l+1} - ... - \omega_{2l-1}$. From the conservation of frequency, $\Delta\omega = \omega$, where ω is the frequency associated with self-energy.

By construction, the propagators directed from the left to right correspond to the greater component of the Green's function, $g^>(k_1, \omega_1), \ldots, g^>(k_l, \omega_l)$ while the ones directed oppositely correspond to the lesser components of the Green's function, $g^<(k_{l+1}, \omega_{l+1}), \ldots, g^<(k_{2l-1}, \omega_{2l-1})$. Therefore, the greater component of the self-energy of a single diagram to the order U^p is given by

$$\Sigma_p^>(\omega) = U^p \int \frac{d^{2l-1}\vec{\omega} d^{2l-1}\vec{k}}{(2\pi)^{4l-2}} \delta(\omega - \Delta\omega) \times g^>(k_1, \omega_1) \cdots g^<(k_{2l-1}, \omega_{2l-1}) \mathcal{F}_p(\vec{k}, \vec{\omega}), \quad \text{(C3)}$$

where $\vec{\omega} = (\omega_1, \ldots, \omega_{2l-1})$ and $\vec{k} = (k_1, \ldots, k_{2l-1})$. The function $\mathcal{F}_p(\vec{k}, \vec{\omega})$ depends on the spatial form of the interactions, $\chi(r)$, and also includes contributions from all the propagators that do not cross the center of the diagram, which include the time-ordered and antitime-ordered components. To keep the notation as simple as possible, we focused on the single species case for the derivation. However, generalization to the multispecies case is straightforward.

Our goal is to find an approximate spread of the self-energy. Therefore, instead of evaluating Eq. (C3), we will estimate its upper bound, $\Sigma_p^>(\omega) \leqslant \tilde{\Sigma}_p^>(\omega)$, which is easier to evaluate. To find the bound, we use the Cauchy-Schwarz inequality, giving rise to

$$\tilde{\Sigma}_p^>(\omega) = U^p \int \frac{d\omega_1 ... d\omega_{2l-1}}{(2\pi)^{2l-1}} \delta(\omega - \Delta\omega) \times \bar{g}^>(\omega_1) \cdots \bar{g}^<(\omega_{2l-1}) \bar{\mathcal{F}}_p(\omega_1, \ldots, \omega_{2l-1}). \quad \text{(C4)}$$

where $\bar{\mathcal{F}}_p(\vec{\omega}) = \sqrt{\int \frac{d^{2l-1}\vec{k}}{(2\pi)^{2l-1}} |\mathcal{F}_p(\vec{k}, \vec{\omega})|^2}$ and $\bar{g}(\omega) = \sqrt{\int \frac{dk}{2\pi} |g(k, \omega)|^2}$. Importantly, the bound in Eq. (C4) is independent of the specific spatial dependence of $\chi(r)$, because it only depends on the averaged value, $\bar{\mathcal{F}}_p(\vec{\omega})$. The result converges as long as $\bar{\mathcal{F}}_p(\vec{\omega})$ is analytic.

Our goal is to estimate $\tilde{\Sigma}^>(\omega)$ for ω away from the support of the noninteracting density of states. The dominant contribution to the self-energy would arise from ladder-shaped diagram, as is shown in Fig. 5(c). Such a diagram has maximal number of lines crossing the center of the diagram, with minimal constraints on the intermediate frequencies.

The unique topology of this diagram allows us to write it as a recursive relation

$$\tilde{\Sigma}_{p+2}^>(\omega) = U^2 \int \frac{d\omega_1 d\omega_2 d\omega_3}{(2\pi)^2} \delta(\omega_3 - \omega + \omega_1 - \omega_2) \times \bar{g}^>(\omega_1) \bar{g}^<(\omega_2) \bar{g}^T(\omega_3) \bar{g}^{\bar{T}}(\omega_3) \Sigma_p^>(\omega_3) \quad \text{(C5)}$$

with the initial condition

$$\tilde{\Sigma}_2^>(\omega) = U^2 \int \frac{d\omega_1 d\omega_2}{(2\pi)^2} \bar{g}^>(\omega_1) \bar{g}^<(\omega_2) \bar{g}^>(\omega - \omega_1 + \omega_2). \quad \text{(C6)}$$

For simplicity, we assume a nearly quasisteady state in which the lesser and greater functions can be approximated by $\bar{g}^>(\omega) \approx i\bar{f}_R^0 \bar{g}_R^\Delta(\omega) + i\bar{f}_L^0 \bar{g}_L^\Delta(\omega)$ and $\bar{g}^<(\omega) \approx -i f_R^0 \bar{g}_R^\Delta(\omega) - i f_L^0 \bar{g}_L^\Delta(\omega)$. The dominant contribution arises from diagrams where each pair of propagators in Eqs. (C5) and (C6) corresponds to the same band, i.e., $\bar{g}^>(\omega_1)\bar{g}^<(\omega_2) \to (f_L\bar{f}_L + f_R\bar{f}_R)\bar{g}_0^\Delta(\omega_1)\bar{g}_0^\Delta(\omega_2)$, where $\bar{g}_0^\Delta(\omega)$ is the density of states of one of the bands shifted to the center of the energy. We also approximate $\bar{g}^T(\omega)\bar{g}^{\bar{T}}(\omega) \approx 1/\omega^2$.

The solution to Eq. (C6), can be written as $\tilde{\Sigma}_2^>(\omega) \approx iU^2 (f_L \bar{f}_L + f_R \bar{f}_R)[\bar{f}_R \tilde{g}_R^\Delta (3W_F, \omega) + \bar{f}_L \tilde{g}_L^\Delta (3W_F, \omega)]$, where $\tilde{g}_\nu^\Delta(d, \omega)$ is a function of width d centered around the νth band. Applying Eq. (C5), we obtain $\tilde{\Sigma}_4^>(\omega) \approx i\frac{U^4}{((3/2)W_F)^2}(f_L\bar{f}_L + f_R\bar{f}_R)^2[\bar{f}_R\tilde{g}_R^\Delta(5W_F, \omega) + \bar{f}_L \tilde{g}_L^\Delta (5W_F, \omega)]$. Similarly, after p iterations, we arrive at $\tilde{\Sigma}_{2p}^>(\omega) \approx \frac{iU^{2p}}{(p!)^2 W_F^{2p-2}}(f_L\bar{f}_L + f_R\bar{f}_R)^p[\bar{f}_R\tilde{g}_R^\Delta((2p+1)W_F, \omega) + \bar{f}_L\tilde{g}_L^\Delta((2p+1)W_F, \omega)]$. We separate the self-energy to $\tilde{\Sigma}_{2p}^>(\omega) = \tilde{\Sigma}_{L,2p}^>(\omega) + \tilde{\Sigma}_{R,2p}^>(\omega)$ where $\tilde{\Sigma}_{\nu,2p}^>(\omega) \approx \frac{iU^{2p}}{(p!)^2 W_F^{2p-2}}(f_L\bar{f}_L + f_R\bar{f}_R)^p \bar{f}_\nu \tilde{g}_\nu^\Delta((2p+1)W_F, \omega)$.

For a distance $|\omega|$ from the left band, the leading order in p is proportional to $p \sim |\omega/W_F|$. Therefore, the bound on the self-energy to this order reads $\tilde{\Sigma}_L^>(\omega) \approx \frac{iU\bar{f}_L}{(\lfloor|\omega/W_F|\rfloor!)^2}[\frac{U^2}{W_F^2}(f_L\bar{f}_L + f_R\bar{f}_R)]^{|\omega|/W_F}$. Using Stirling's approximation $p! \approx p^p$, we obtain $\tilde{\Sigma}_L^>(\omega) \approx iU\bar{f}_L[\frac{U^2}{\omega^2}(f_L\bar{f}_L + f_R\bar{f}_R)]^{|\omega|/W_F}$. For ω of the order of Δ, we arrive at $\Sigma_L^>(\omega) \leqslant \tilde{\Sigma}_L^>(\omega) \propto iU\bar{f}_L e^{-|\omega|/\xi}$, where

$$\xi \approx -W_F / \ln\left(\frac{U^2}{\Delta^2}[f_L\bar{f}_L + f_R\bar{f}_R]\right). \quad \text{(C7)}$$

Similarly, the lesser component of the self-energy reads $\Sigma_L^<(\omega) \propto -iU f_L e^{-|\omega|/\xi}$. Therefore, $\Sigma^\Delta = i\Sigma^> - i\Sigma^< \propto Ue^{-|\omega|/\xi}$. Using Eq. (C2), we obtain

$$G_L^\Delta(\omega) \propto e^{-|\omega|/\xi}. \quad \text{(C8)}$$

A similar calculation near the upper band leads to the same energy scale for the broadening.

APPENDIX D: KINETIC EQUATION

In this section, we derive the kinetic equation for the occupation probabilities, defined in Eq. (5), and demonstrate that this equation is solved by constant occupations of the bands $f_L = f_L^0$ and $f_R = f_R^0$, up to terms proportional to $\mathcal{O}(\delta f e^{-\Delta/\xi})$, where $\delta f = f_L^0 - f_R^0$. This means that the fixed point of the kinetic equation to the order $e^{-\Delta/\xi}$ corresponds to an infinite temperature distribution in each of the bands. If these terms are included, the fixed point is a global infinite temperature state, in which $\delta f = 0$.

To derive the kinetic equation, we substitute Eq. (5), in Eq. (3b). Before, performing the substitution, we rewrite Eq. (3b) in the frequency-momentum domain by performing the Wigner transformation of the time-frequency domain, yielding

$$[\omega - H_0(k,t) \,\natural\, G^<(k;\omega,t)] = \Sigma^R \circ G^< - G^< \circ \Sigma^A - G^R \circ \Sigma^< + \Sigma^< \circ G^A. \quad \text{(D1)}$$

Here, "$\circ$" denotes the Moyal and matrix product and $[A \,\natural\, B] = A \circ B - B \circ A$. To the first order in the derivatives and commutators the Moyal commutator reads $[A \,\natural\, B] = [A, B] + i\partial_t A \partial_\omega B - i\partial_w A \partial_t B$. Our goal is to derive an equation for $\dot{f}_L$

and $\dot{f}_R$ without imposing the on-shell approximation, which otherwise would not include the interband transitions occurring off shell. Equation (D1) describes the time evolution of $G^<$, which includes time evolutions of both the spectral function and the occupations [see Eq. (5)]. On the other hand, the evolution of G^Δ alone can be derived from Eq. (3a), and reads

$$[\omega - H_0(k,t) \,\natural\, G^\Delta(k;\omega,t)] = \Sigma^R \circ G^\Delta - G^\Delta \circ \Sigma^A - G^R \circ \Sigma^\Delta + \Sigma^\Delta \circ G^A. \quad \text{(D2)}$$

To separate the kinetic equation for f_L from the kinetic equation for G^Δ, we define $\mathcal{I}_L(k;\omega,t) \equiv [\omega - H_0 \,\natural\, G^<] + f_L \circ [\omega - H_0 \,\natural\, G^\Delta]$. Evaluating the left hand side of Eqs. (D1) and (D2), we obtain

$$\mathcal{I}_L = [\omega - H_0 \,\natural\, G^< + f_L \circ G^\Delta] - [\omega - H_0 \,\natural\, f_L] \circ G^\Delta. \quad \text{(D3)}$$

To simplify, we rewrite Eq. (5) as $G^< = -f_L \circ G_L^\Delta - f_R \circ G_R^\Delta + \delta G^<$, where $\delta G^< = [f_L \,\natural\, G_L^R] + [f_R \,\natural\, G_R^R]$. Therefore, $G^< + f_L \circ G^\Delta = \delta f \circ G_R^\Delta + \delta G^<$. To simplify even further, we assume a close to steady state, such that we can keep only the first order terms in the derivatives and commutators of f_ν. With this assumption $\delta G^<$ is already given to the leading order and its Moyal commutator will be of higher order and thus can be neglected. In addition, focusing on $\omega \approx -\Delta/2$, the spectral function scales as $G_R^\Delta \approx e^{-\Delta/\xi}$ [see Eq. (C8)]. Therefore, this term can be neglected compared to $f_L \circ G_L^\Delta$. With these approximations and explicitly computing the Moyal commutator of f_L in Eq. (D3) to the leading order, we obtain

$$\mathcal{I}_L = (i\dot{f}_L + i\dot{H}_0 \partial_\omega f_L - [H_0, f_L]) G_L^\Delta. \quad \text{(D4)}$$

Equation (D4) is essentially the left hand side of the Boltzmann-like equation (up to the band-renormalization terms discussed below).

Similarly, we evaluate $\mathcal{I}_L$ using the right hand side of Eqs. (D1) and (D2), yielding the collision term (and band-renormalization terms). An explicit calculation yields

$$\begin{aligned}\mathcal{I}_L = {} & G^< \circ \Sigma^\Delta - G^\Delta \circ \Sigma^< \\ & + [\Sigma^R \,\natural\, G^< + f_L \circ G^\Delta] - [\Sigma^R \,\natural\, f_L] \circ G^\Delta \\ & + [\Sigma^< + f_L \circ \Sigma^\Delta \,\natural\, G^A] - [f_L \,\natural\, G^A] \circ \Sigma^\Delta. \end{aligned} \quad \text{(D5)}$$

Evaluation of Eq. (D5) in a generic state is complex and is performed in the numerical part. As a first order check, we will verify that the quasisteady state, given in Eq. (6), corresponding to an infinite temperature state for each of the bands $f_\nu = f_\nu^0$, with $f_L^0 \neq f_R^0$ almost nullifies the collision integral and estimate the timescale for the full thermalization of the system to an infinite temperature state (in which $f_R^0 = f_L^0$). Under the assumption of constant occupations, Eq. (D5) simplifies to

$$\begin{aligned}\mathcal{I}_L = {} & \delta f \left(G_R^\Delta \circ \Sigma_L^\Delta - G_L^\Delta \circ \Sigma_R^\Delta\right) \\ & + [\Sigma^R \,\natural\, \delta f G_R^\Delta] + [\delta f \Sigma_R^\Delta \,\natural\, G^A]. \end{aligned} \quad \text{(D6)}$$

Here, we denote by $\Sigma_L(\omega)$ the self-energy near $\omega = -\Delta/2$, and similarly $\Sigma_R(\omega)$, denotes the self-energy near $\omega = \Delta/2$. We also used $\Sigma_L^< \approx -if_L^0 \Sigma_L^\Delta$ and $\Sigma_R^< \approx -if_R^0 \Sigma_R^\Delta$. Importantly, all the terms in $\mathcal{I}_L$ are proportional to Δf and to either G_R^Δ or Σ_R^Δ, that are exponentially small near $\omega = -\Delta/2$. This exponentially small value of $\mathcal{I}_L$ is proportional to the rate of thermalization to the infinite temperature state, in which $\delta f = 0$. In this state Eq. (D6) becomes identically zero, $\mathcal{I}_L = 0$.

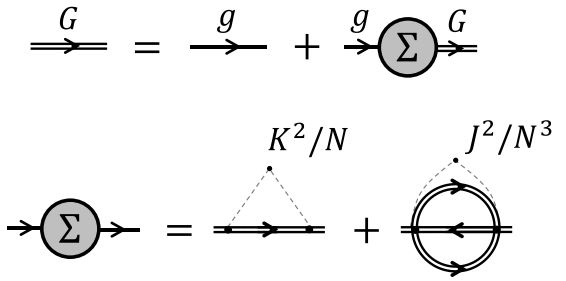

FIG. 6. Self-consistent relations for a Thouless pump with SYK interactions. Single lines represent the noninteracting Green's function $g_{ss'}(k;t,t')$. Double lines represent the renormalized Green's functions $G_{ss'}(k;t,t')$.

APPENDIX E: DETAILS OF THE NUMERICAL SIMULATION

Here, we present the details of the numerical simulation of the time evolution of the Kadanoff-Baym equations [see Eq. (3)]. The time evolution is performed with respect to the SYK Hamiltonian, given in Eq. (2), with $N \to \infty$. To stabilize the numerics in the weakly interacting limit, we added a weak random quadratic term

$$\hat{\mathcal{H}}_{\text{SYK}-2} = \sum_{j,\alpha\beta} K_{\alpha\beta} \hat{c}_{j\alpha}^\dagger \hat{c}_{j\beta} + \text{H.c.}, \quad \text{(E1)}$$

where $\overline{K_{\alpha\beta}} = 0$ and $\overline{K_{\alpha\beta}^2} = K^2/N$.

Instead of evolving in time the G^R and $G^<$ functions, as appears in Eq. (3), we found it more convenient to evolve the retarded G^R, and Keldysh components G^K. The latter is defined as

$$G_{ss'}^K(k;t,t') = G_{ss'}^>(k;t,t') + G_{ss'}^<(k;t,t'). \quad \text{(E2)}$$

The Kadanoff-Baym equations for these two components read

$$[i\partial_t - H_0(t)] G^R = \delta(t-t') + \Sigma^R \circ G^R, \quad \text{(E3a)}$$

$$[i\partial_t - H_0(t)] G^K = \Sigma^R \circ G^K + \Sigma^K \circ G^A. \quad \text{(E3b)}$$

The disorder-averaged self-energy for the chain of SYK dots with SYK-4 [Eq. (2)] and SYK-2 [Eq. (E1)] interactions can be written in the self-consistent form. The diagrammatic structure of the self-energy to the leading order in N is shown in Fig. 6 [119]. As follows from this diagram, the greater and lesser components of the self-energy are given by

$$\begin{aligned}\Sigma_{ss'}^{\gtrless}(x;t,t') = {} & K^2 G_{ss'}^{\gtrless}(x;t,t') \\ & + J^2 [G_{ss'}^{\gtrless}(x;t,t')]^2 G_{s's}^{\lessgtr}(-x;t',t). \end{aligned} \quad \text{(E4)}$$

Here, x is obtained from the Fourier transform of the momentum, k, index. The retarded and Keldysh Green's functions G^R and G^K [appearing in Eq. (E3)] are related

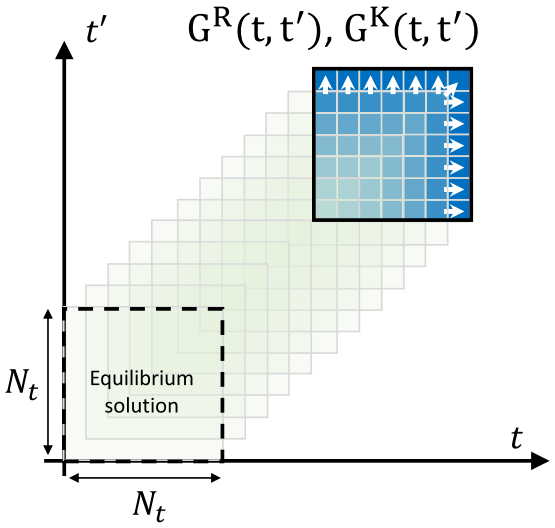

FIG. 7. Time evolution of the retarded and Keldysh Green's functions according to the Kadanoff-Baym equations [Eqs. (E3)]. The square in the bottom left corner represents the initial conditions for the Green's function, $G_{\rm eq}(t,t')$. At each step of the evolution a new row, column, and cell on the diagonal are added to the matrix, corresponding to $G(t_0+\delta t,t)$, $G(t,t_0+\delta t)$, and $G(t_0+\delta t,t_0+\delta t)$.

to $G^{\gtrless}$ via $G^R_{ss'}(k;t,t') = \theta(t-t')[G^>_{ss'}(k;t,t') - G^<_{ss'}(k;t,t')]$ and Eq. (E2). In turn, the inverse relations read $G^{\gtrless} = \frac{1}{2}[G^K \pm (G^R - G^A)]$, where $G^A_{ss'}(k;t,t') = G^R_{s's}(k;t',t)^\dagger$. The relations for the self-energy are similar, with G replaced by Σ.

1. Equilibrium solution

Equations (E3) and (E4) constitute a set of integro-differential equations which determine the time evolution of the Green's functions. Initial conditions for this time evolution are set by the state ρ_0, corresponding to equilibrium with an inverse temperature β_0 and Hamiltonian $\hat{\mathcal{H}}(0)$. Due to invariance to time translations in equilibrium, the equilibrium Green's functions depend only on the time difference $\Delta t = t - t'$. To find the equilibrium solution, we evaluate Eq. (E3a) for $H_0(t)$ at $t = 0$ and transform Δt to the frequency space ω, giving rise to

$$[\omega - H_0(0)]G^R(\omega) = 1 + \Sigma^R(\omega)G^R(\omega). \tag{E5}$$

Furthermore, Eq. (E3b) is trivially satisfied in equilibrium, due to the fluctuation-dissipation theorem [144,145,152]:

$$G^K_{ss'}(\omega) = F(\omega)\big[G^R_{ss'}(\omega) - G^A_{ss'}(\omega)\big], \tag{E6}$$

where $F(\omega) = \tanh(\beta_0\omega/2)$. The equilibrium Green's function is obtained from the self-consistent solution of Eqs. (E4)–(E6).

2. Time evolution

Having found an equilibrium solution, $G^R_{\rm eq}(k;t-t')$ and $G^K_{\rm eq}(k;t-t')$, we rearrange the vectors into matrices $[G^R_{\rm eq}]_{ss'}(k;t,t')$ and $[G^K_{\rm eq}]_{ss'}(k;t,t')$ of size $N_t \times N_t$ in the time domain and 2×2 in the sublattice space, for a vector of crystal momenta of size L. In our simulations, we used $N_t = 3000$ (smaller values of N_t are used to vary $\delta\omega$ and δt), and $L = 50$. We used the equilibrium solution as the starting point of the simulation to propagate the Green's functions by one time step δt in each iteration according to Eq. (E3) [148] (see Fig. 7). In particular, given $G^R(t_0,t')$, we evolve G^R according to

$$G^R(t_0+\delta t,t') = U_0(t_0)\left[G^R(t_0,t') - \frac{i}{2}\delta_{t,t'}\right] - i\delta t I^R(t') \tag{E7}$$

for $t' \leqslant t_0$; $G^R(t,t_0+\delta t) = 0$ for $t \leqslant t_0$; and $G^R(t_0+\delta t,t_0+\delta t) = G^R(t_0,t_0)$. Here we defined $U_0(t) = e^{-i\delta t H_0(t)}$ and $I^R(t') = \int \Sigma^R(t_0,s)G^R(s,t')ds$.

To optimize the efficiency of the simulation, we keep the overall size of the matrices constant. Therefore, for each new element of the Green's function calculated in the future, we erase one element in the past. Such a truncation of the Green's function fixes the required memory of the simulation and significantly reduces the computational resources used. The attached movies in the Supplemental Material demonstrate the time evolution of the lesser function $G^<(k,\omega,\bar{t})$ and the spectral function $G^\Delta(k,\omega,\bar{t})$, as a function of $\bar{t}$ [138].

[1] T. Oka and H. Aoki, Photovoltaic Hall effect in graphene, Phys. Rev. B **79**, 081406(R) (2009).

[2] T. Kitagawa, E. Berg, M. Rudner, and E. Demler, Topological characterization of periodically driven quantum systems, Phys. Rev. B **82**, 235114 (2010).

[3] N. H. Lindner, G. Refael, and V. Galitski, Floquet topological insulator in semiconductor quantum wells, Nat. Phys. **7**, 490 (2011).

[4] J. Dalibard, F. Gerbier, G. Juzeliunas, and P. Öhberg, *Colloquium:* Artificial gauge potentials for neutral atoms, Rev. Mod. Phys. **83**, 1523 (2011).

[5] A. Gómez-León and G. Platero, Floquet-Bloch theory and topology in periodically driven lattices, Phys. Rev. Lett. **110**, 200403 (2013).

[6] D. A. Huse, R. Nandkishore, V. Oganesyan, A. Pal, and S. L. Sondhi, Localization-protected quantum order, Phys. Rev. B **88**, 014206 (2013).

[7] M. S. Rudner, N. H. Lindner, E. Berg, and M. Levin, Anomalous edge states and the bulk-edge correspondence for periodically driven two-dimensional systems, Phys. Rev. X **3**, 031005 (2013).

[8] H. Dehghani, T. Oka, and A. Mitra, Dissipative Floquet topological systems, Phys. Rev. B **90**, 195429 (2014).

[9] L. E. F. Foa Torres, P. M. Perez-Piskunow, C. A. Balseiro, and G. Usaj, Multiterminal conductance of a Floquet topological insulator, Phys. Rev. Lett. **113**, 266801 (2014).

[10] G. Usaj, P. M. Perez-Piskunow, L. E. F. Foa Torres, and C. A. Balseiro, Irradiated graphene as a tunable Floquet topological insulator, Phys. Rev. B **90**, 115423 (2014).

[11] A. Chandran, V. Khemani, C. R. Laumann, and S. L. Sondhi, Many-body localization and symmetry-protected topological order, Phys. Rev. B **89**, 144201 (2014).

[12] N. Goldman, G. Juzeliūnas, P. Öhberg, and I. B. Spielman, Light-induced gauge fields for ultracold atoms, Rep. Prog. Phys. **77**, 126401 (2014).

[13] A. G. Grushin, Á. Gómez-León, and T. Neupert, Floquet fractional Chern insulators, Phys. Rev. Lett. **112**, 156801 (2014).

[14] A. Kundu, H. A. Fertig, and B. Seradjeh, Effective theory of Floquet topological transitions, Phys. Rev. Lett. **113**, 236803 (2014).

[15] P. M. Perez-Piskunow, L. E. F. Foa Torres, and G. Usaj, Hierarchy of Floquet gaps and edge states for driven honeycomb lattices, Phys. Rev. A **91**, 043625 (2015).

[16] V. Dal Lago, M. Atala, and L. E. F. Foa Torres, Floquet topological transitions in a driven one-dimensional topological insulator, Phys. Rev. A **92**, 023624 (2015).

[17] F. Nathan and M. S. Rudner, Topological singularities and the general classification of Floquet-Bloch systems, New J. Phys. **17**, 125014 (2015).

[18] V. Khemani, A. Lazarides, R. Moessner, and S. L. Sondhi, Phase structure of driven quantum systems, Phys. Rev. Lett. **116**, 250401 (2016).

[19] C. W. von Keyserlingk and S. L. Sondhi, Phase structure of one-dimensional interacting Floquet systems. II. Symmetry-broken phases, Phys. Rev. B **93**, 245146 (2016).

[20] C. W. von Keyserlingk and S. L. Sondhi, Phase structure of one-dimensional interacting Floquet systems. I. Abelian symmetry-protected topological phases, Phys. Rev. B **93**, 245145 (2016).

[21] D. V. Else and C. Nayak, Classification of topological phases in periodically driven interacting systems, Phys. Rev. B **93**, 201103(R) (2016).

[22] H. C. Po, L. Fidkowski, T. Morimoto, A. C. Potter, and A. Vishwanath, Chiral Floquet phases of many-body localized bosons, Phys. Rev. X **6**, 041070 (2016).

[23] A. C. Potter, T. Morimoto, and A. Vishwanath, Classification of interacting topological Floquet phases in one dimension, Phys. Rev. X **6**, 041001 (2016).

[24] A. Eckardt, *Colloquium:* Atomic quantum gases in periodically driven optical lattices, Rev. Mod. Phys. **89**, 011004 (2017).

[25] R. Roy and F. Harper, Periodic table for Floquet topological insulators, Phys. Rev. B **96**, 155118 (2017).

[26] R. Roy and F. Harper, Floquet topological phases with symmetry in all dimensions, Phys. Rev. B **95**, 195128 (2017).

[27] F. Harper and R. Roy, Floquet topological order in interacting systems of bosons and fermions, Phys. Rev. Lett. **118**, 115301 (2017).

[28] Z. Gong, Y. Ashida, K. Kawabata, K. Takasan, S. Higashikawa, and M. Ueda, Topological phases of non-Hermitian systems, Phys. Rev. X **8**, 031079 (2018).

[29] I. Esin, M. S. Rudner, G. Refael, and N. H. Lindner, Quantized transport and steady states of Floquet topological insulators, Phys. Rev. B **97**, 245401 (2018).

[30] T. Ozawa, H. M. Price, A. Amo, N. Goldman, M. Hafezi, L. Lu, M. C. Rechtsman, D. Schuster, J. Simon, O. Zilberberg, and I. Carusotto, Topological photonics, Rev. Mod. Phys. **91**, 015006 (2019).

[31] N. R. Cooper, J. Dalibard, and I. B. Spielman, Topological bands for ultracold atoms, Rev. Mod. Phys. **91**, 015005 (2019).

[32] F. Tonielli, J. C. Budich, A. Altland, and S. Diehl, Topological field theory far from equilibrium, Phys. Rev. Lett. **124**, 240404 (2020).

[33] M. S. Rudner and N. H. Lindner, Band structure engineering and non-equilibrium dynamics in Floquet topological insulators, Nat. Rev. Phys. **2**, 229 (2020).

[34] F. Harper, R. Roy, M. S. Rudner, and S. L. Sondhi, Topology and broken symmetry in Floquet systems, Annu. Rev. Condens. Matter Phys. **11**, 345 (2020).

[35] R.-X. Zhang and Z.-C. Yang, Tunable fragile topology in Floquet systems, Phys. Rev. B **103**, L121115 (2021).

[36] D. P. Arovas, R. Schrieffer, F. Wilczek, and A. Zee, Statistical mechanics of anyons, Nucl. Phys. B **251**, 117 (1985).

[37] A. Altland and M. R. Zirnbauer, Nonstandard symmetry classes in mesoscopic normal-superconducting hybrid structures, Phys. Rev. B **55**, 1142 (1997).

[38] A. Kitaev, Anyons in an exactly solved model and beyond, Ann. Phys. (NY) **321**, 2 (2006).

[39] A. Stern, Anyons and the quantum Hall effect–A pedagogical review, Ann. Phys. (NY) **323**, 204 (2008).

[40] C. Nayak, S. H. Simon, A. Stern, M. Freedman, and S. Das Sarma, Non-Abelian anyons and topological quantum computation, Rev. Mod. Phys. **80**, 1083 (2008).

[41] A. Kitaev, Periodic table for topological insulators and superconductors, AIP Conf. Proc. **1134**, 22 (2009).

[42] M. Z. Hasan and C. L. Kane, *Colloquium:* Topological insulators, Rev. Mod. Phys. **82**, 3045 (2010).

[43] X.-L. Qi and S.-C. Zhang, Topological insulators and superconductors, Rev. Mod. Phys. **83**, 1057 (2011).

[44] L. Fidkowski and A. Kitaev, Topological phases of fermions in one dimension, Phys. Rev. B **83**, 075103 (2011).

[45] Y. Ren, Z. Qiao, and Q. Niu, Topological phases in two-dimensional materials: A review, Rep. Prog. Phys. **79**, 066501 (2016).

[46] C. K. Chiu, J. C. Y. Teo, A. P. Schnyder, and S. Ryu, Classification of topological quantum matter with symmetries, Rev. Mod. Phys. **88**, 035005 (2016).

[47] X.-G. Wen, *Colloquium:* Zoo of quantum-topological phases of matter, Rev. Mod. Phys. **89**, 041004 (2017).

[48] M. Aidelsburger, M. Atala, S. Nascimbène, S. Trotzky, Y.-A. Chen, and I. Bloch, Experimental realization of strong effective magnetic fields in an optical lattice, Phys. Rev. Lett. **107**, 255301 (2011).

[49] M. C. Rechtsman, J. M. Zeuner, Y. Plotnik, Y. Lumer, D. Podolsky, F. Dreisow, S. Nolte, M. Segev, and A. Szameit, Photonic Floquet topological insulators, Nature (London) **496**, 196 (2013).

[50] M. Aidelsburger, M. Lohse, C. Schweizer, M. Atala, J. T. Barreiro, S. Nascimbène, N. R. Cooper, I. Bloch, and N. Goldman, Measuring the Chern number of Hofstadter bands with ultracold bosonic atoms, Nat. Phys. **11**, 162 (2015).

[51] G. Jotzu, M. Messer, R. Desbuquois, M. Lebrat, T. Uehlinger, D. Greif, and T. Esslinger, Experimental realization of the topological Haldane model with ultracold fermions, Nature (London) **515**, 237 (2014).

[52] R. Fleury, A. B. Khanikaev, and A. Alù, Floquet topological insulators for sound, Nat. Commun. **7**, 11744 (2016).

[53] D. N. Basov, R. D. Averitt, and D. Hsieh, Towards properties on demand in quantum materials, Nat. Mater. **16**, 1077 (2017).

[54] T. Oka and S. Kitamura, Floquet engineering of quantum materials, Annu. Rev. Condens. Matter Phys. **10**, 387 (2019).

[55] J. W. McIver, B. Schulte, F.-U. Stein, T. Matsuyama, G. Jotzu, G. Meier, and A. Cavalleri, Light-induced anomalous Hall effect in graphene, Nat. Phys. **16**, 38 (2020).

[56] J.-Y. Shan, M. Ye, H. Chu, S. Lee, J.-G. Park, L. Balents, and D. Hsieh, Giant modulation of optical nonlinearity by Floquet engineering, Nature (London) **600**, 235 (2021).

[57] S. Mukherjee and M. C. Rechtsman, Observation of unidirectional solitonlike edge states in nonlinear floquet topological insulators, Phys. Rev. X **11**, 041057 (2021).

[58] D. V. Else, B. Bauer, and C. Nayak, Floquet time crystals, Phys. Rev. Lett. **117**, 090402 (2016).

[59] P. Titum, E. Berg, M. S. Rudner, G. Refael, and N. H. Lindner, Anomalous Floquet-Anderson insulator as a nonadiabatic quantized charge pump, Phys. Rev. X **6**, 021013 (2016).

[60] Y.-G. Peng, C.-Z. Qin, D.-G. Zhao, Y.-X. Shen, X.-Y. Xu, M. Bao, H. Jia, and X.-F. Zhu, Experimental demonstration of anomalous Floquet topological insulator for sound, Nat. Commun. **7**, 13368 (2016).

[61] J. Zhang, P. W. Hess, A. Kyprianidis, P. Becker, A. Lee, J. Smith, G. Pagano, I.-D. Potirniche, A. C. Potter, A. Vishwanath, N. Y. Yao, and C. Monroe, Observation of a discrete time crystal, Nature (London) **543**, 217 (2017).

[62] S. Choi, J. Choi, R. Landig, G. Kucsko, H. Zhou, J. Isoya, F. Jelezko, S. Onoda, H. Sumiya, V. Khemani, C. Von Keyserlingk, N. Y. Yao, E. Demler, and M. D. Lukin, Observation of discrete time-crystalline order in a disordered dipolar many-body system, Nature (London) **543**, 221 (2017).

[63] L. J. Maczewsky, J. M. Zeuner, S. Nolte, and A. Szameit, Observation of photonic anomalous Floquet topological insulators, Nat. Commun. **8**, 13756 (2017).

[64] S. Mukherjee, A. Spracklen, M. Valiente, E. Andersson, P. Öhberg, N. Goldman, and R. R. Thomson, Experimental observation of anomalous topological edge modes in a slowly driven photonic lattice, Nat. Commun. **8**, 13918 (2017).

[65] F. Nathan, D. Abanin, E. Berg, N. H. Lindner, and M. S. Rudner, Anomalous Floquet insulators, Phys. Rev. B **99**, 195133 (2019).

[66] K. Wintersperger, C. Braun, F. N. Ünal, A. Eckardt, M. D. Liberto, N. Goldman, I. Bloch, and M. Aidelsburger, Realization of an anomalous Floquet topological system with ultracold atoms, Nat. Phys. **16**, 1058 (2020).

[67] S. Afzal, T. J. Zimmerling, Y. Ren, D. Perron, and V. Van, Realization of anomalous Floquet insulators in strongly coupled nanophotonic lattices, Phys. Rev. Lett. **124**, 253601 (2020).

[68] I. Esin, M. S. Rudner, and N. H. Lindner, Floquet metal-to-insulator phase transitions in semiconductor nanowires, Sci. Adv. **6**, eaay4922 (2020).

[69] I. Esin, G. K. Gupta, E. Berg, M. S. Rudner, and N. H. Lindner, Electronic Floquet gyro-liquid crystal, Nat. Commun. **12**, 5299 (2021).

[70] D. J. Thouless, Quantization of particle transport, Phys. Rev. B **27**, 6083 (1983).

[71] Q. Niu and D. J. Thouless, Quantised adiabatic charge transport in the presence of substrate disorder and many-body interaction, J. Phys. A **17**, 2453 (1984).

[72] Q. Niu, Towards a quantum pump of electric charges, Phys. Rev. Lett. **64**, 1812 (1990).

[73] P. W. Brouwer, Scattering approach to parametric pumping, Phys. Rev. B **58**, R10135(R) (1998).

[74] M. Switkes, C. M. Marcus, K. Campman, and A. C. Gossard, An adiabatic quantum electron pump, Science **283**, 1905 (1999).

[75] B. L. Altshuler and L. I. Glazman, Pumping electrons, Science **283**, 1864 (1999).

[76] C.-H. Chern, S. Onoda, S. Murakami, and N. Nagaosa, Quantum charge pumping and electric polarization in Anderson insulators, Phys. Rev. B **76**, 035334 (2007).

[77] D. Xiao, M.-C. Chang, and Q. Niu, Berry phase effects on electronic properties, Rev. Mod. Phys. **82**, 1959 (2010).

[78] D. Meidan, T. Micklitz, and P. W. Brouwer, Topological classification of adiabatic processes, Phys. Rev. B **84**, 195410 (2011).

[79] Y. H. Wang, H. Steinberg, P. Jarillo-Herrero, and N. Gedik, Observation of Floquet-Bloch states on the surface of a topological insulator, Science **342**, 453 (2013).

[80] M. W. Keller, A. L. Eichenberger, J. M. Martinis, and N. M. Zimmerman, A capacitance standard based on counting electrons, Science **285**, 1706 (1999).

[81] F. Piquemal, A. Bounouh, L. Devoille, N. Feltin, O. Thevenot, and G. Trapon, Fundamental electrical standards and the quantum metrological triangle, C. R. Phys. **5**, 857 (2004).

[82] M. D. Blumenthal, B. Kaestner, L. Li, S. Giblin, T. J. B. M. Janssen, M. Pepper, D. Anderson, G. Jones, and D. A. Ritchie, Gigahertz quantized charge pumping, Nat. Phys. **3**, 343 (2007).

[83] S. P. Giblin, M. Kataoka, J. D. Fletcher, P. See, T. J. B. M. Janssen, J. P. Griffiths, G. A. C. Jones, I. Farrer, and D. A. Ritchie, Towards a quantum representation of the ampere using single electron pumps, Nat. Commun. **3**, 930 (2012).

[84] J. P. Pekola, O.-P. Saira, V. F. Maisi, A. Kemppinen, M. Möttönen, Y. A. Pashkin, and D. V. Averin, Single-electron current sources: Toward a refined definition of the ampere, Rev. Mod. Phys. **85**, 1421 (2013).

[85] J. D. Fletcher, P. See, H. Howe, M. Pepper, S. P. Giblin, J. P. Griffiths, G. A. C. Jones, I. Farrer, D. A. Ritchie, T. J. B. M. Janssen, and M. Kataoka, Clock-controlled emission of single-electron wave packets in a solid-state circuit, Phys. Rev. Lett. **111**, 216807 (2013).

[86] N. Ubbelohde, F. Hohls, V. Kashcheyevs, T. Wagner, L. Fricke, B. Kästner, K. Pierz, H. W. Schumacher, and R. J. Haug, Partitioning of on-demand electron pairs, Nat. Nanotechnol. **10**, 46 (2015).

[87] N. Johnson, J. D. Fletcher, D. A. Humphreys, P. See, J. P. Griffiths, G. A. C. Jones, I. Farrer, D. A. Ritchie, M. Pepper, T. J. B. M. Janssen, and M. Kataoka, Ultrafast voltage sampling using single-electron wavepackets, Appl. Phys. Lett. **110**, 102105 (2017).

[88] Y. E. Kraus, Y. Lahini, Z. Ringel, M. Verbin, and O. Zilberberg, Topological states and adiabatic pumping in quasicrystals, Phys. Rev. Lett. **109**, 106402 (2012).

[89] C. Schweizer, M. Lohse, R. Citro, and I. Bloch, Spin pumping and measurement of spin currents in optical superlattices, Phys. Rev. Lett. **117**, 170405 (2016).
[90] M. Lohse, C. Schweizer, O. Zilberberg, M. Aidelsburger, and I. Bloch, A Thouless quantum pump with ultracold bosonic atoms in an optical superlattice, Nat. Phys. **12**, 350 (2016).
[91] S. Nakajima, T. Tomita, S. Taie, T. Ichinose, H. Ozawa, L. Wang, M. Troyer, and Y. Takahashi, Topological Thouless pumping of ultracold fermions, Nat. Phys. **12**, 296 (2016).
[92] O. Zilberberg, S. Huang, J. Guglielmon, M. Wang, K. P. Chen, Y. E. Kraus, and M. C. Rechtsman, Photonic topological boundary pumping as a probe of 4D quantum Hall physics, Nature (London) **553**, 59 (2018).
[93] M. Lohse, C. Schweizer, H. M. Price, O. Zilberberg, and I. Bloch, Exploring 4D quantum Hall physics with a 2D topological charge pump, Nature (London) **553**, 55 (2018).
[94] A. Cerjan, M. Wang, S. Huang, K. P. Chen, and M. C. Rechtsman, Thouless pumping in disordered photonic systems, Light Sci. Appl. **9**, 178 (2020).
[95] S. Nakajima, N. Takei, K. Sakuma, Y. Kuno, P. Marra, and Y. Takahashi, Competition and interplay between topology and quasi-periodic disorder in Thouless pumping of ultracold atoms, Nat. Phys. **17**, 844 (2021).
[96] M. Jürgensen, S. Mukherjee, and M. C. Rechtsman, Quantized nonlinear Thouless pumping, Nature (London) **596**, 63 (2021).
[97] J. Minguzzi, Z. Zhu, K. Sandholzer, A.-S. Walter, K. Viebahn, and T. Esslinger, Topological pumping in a Floquet-Bloch band, Phys. Rev. Lett. **129**, 053201 (2022).
[98] A. Lazarides, A. Das, and R. Moessner, Equilibrium states of generic quantum systems subject to periodic driving, Phys. Rev. E **90**, 012110 (2014).
[99] L. D'Alessio and M. Rigol, Long-time behavior of isolated periodically driven interacting lattice systems, Phys. Rev. X **4**, 041048 (2014).
[100] P. Ponte, A. Chandran, Z. Papić, and D. A. Abanin, Periodically driven ergodic and many-body localized quantum systems, Ann. Phys. (NY) **353**, 196 (2015).
[101] M. Bukov, L. D'Alessio, and A. Polkovnikov, Universal high-frequency behavior of periodically driven systems: From dynamical stabilization to Floquet engineering, Adv. Phys. **64**, 139 (2015).
[102] A. Eckardt and E. Anisimovas, High-frequency approximation for periodically driven quantum systems from a Floquet-space perspective, New J. Phys. **17**, 093039 (2015).
[103] D. A. Abanin, W. De Roeck, and F. Huveneers, Exponentially slow heating in periodically driven many-body systems, Phys. Rev. Lett. **115**, 256803 (2015).
[104] M. Bukov, M. Heyl, D. A. Huse, and A. Polkovnikov, Heating and many-body resonances in a periodically driven two-band system, Phys. Rev. B **93**, 155132 (2016).
[105] T. Kuwahara, T. Mori, and K. Saito, Floquet-Magnus theory and generic transient dynamics in periodically driven many-body quantum systems, Ann. Phys. (NY) **367**, 96 (2016).
[106] D. V. Else, B. Bauer, and C. Nayak, Prethermal phases of matter protected by time-translation symmetry, Phys. Rev. X **7**, 011026 (2017).
[107] D. Abanin, W. De Roeck, W. W. Ho, and F. Huveneers, A rigorous theory of many-body prethermalization for periodically driven and closed quantum systems, Commun. Math. Phys. **354**, 809 (2017).
[108] M. Reitter, J. Näger, K. Wintersperger, C. Sträter, I. Bloch, A. Eckardt, and U. Schneider, Interaction dependent heating and atom loss in a periodically driven optical lattice, Phys. Rev. Lett. **119**, 200402 (2017).
[109] T. Mori, Floquet prethermalization in periodically driven classical spin systems, Phys. Rev. B **98**, 104303 (2018).
[110] O. Howell, P. Weinberg, D. Sels, A. Polkovnikov, and M. Bukov, Asymptotic prethermalization in periodically driven classical spin chains, Phys. Rev. Lett. **122**, 010602 (2019).
[111] M. Vogl, P. Laurell, A. D. Barr, and G. A. Fiete, Flow equation approach to periodically driven quantum systems, Phys. Rev. X **9**, 021037 (2019).
[112] C. Kuhlenkamp and M. Knap, Periodically driven Sachdev-Ye-Kitaev models, Phys. Rev. Lett. **124**, 106401 (2020).
[113] C. Fleckenstein and M. Bukov, Thermalization and prethermalization in periodically kicked quantum spin chains, Phys. Rev. B **103**, 144307 (2021).
[114] N. H. Lindner, E. Berg, and M. S. Rudner, Universal chiral quasisteady states in periodically driven many-body systems, Phys. Rev. X **7**, 011018 (2017).
[115] T. Gulden, E. Berg, M. S. Rudner, and N. H Lindner, Exponentially long lifetime of universal quasi-steady states in topological Floquet pumps, SciPost Phys. **9**, 015 (2020).
[116] R. Gawatz, A. C. Balram, E. Berg, N. H. Lindner, and M. S. Rudner, Prethermalization and entanglement dynamics in interacting topological pumps, Phys. Rev. B **105**, 195118 (2022).
[117] S. Sachdev and J. Ye, Gapless spin-fluid ground state in a random quantum Heisenberg magnet, Phys. Rev. Lett. **70**, 3339 (1993).
[118] A. Kitaev, A simple model of quantum holography, Talks at KITP, 7 April 2015, http://online.kitp.ucsb.edu/online/entangled15/kitaev/; 27 May 2015, http://online.kitp.ucsb.edu/online/entangled15/kitaev2/.
[119] J. Maldacena and D. Stanford, Remarks on the Sachdev-Ye-Kitaev model, Phys. Rev. D **94**, 106002 (2016).
[120] X.-Y. Song, C.-M. Jian, and L. Balents, Strongly correlated metal built from Sachdev-Ye-Kitaev models, Phys. Rev. Lett. **119**, 216601 (2017).
[121] D. Chowdhury, Y. Werman, E. Berg, and T. Senthil, Translationally invariant non-Fermi-liquid metals with critical Fermi surfaces: Solvable models, Phys. Rev. X **8**, 031024 (2018).
[122] A. A. Patel, J. McGreevy, D. P. Arovas, and S. Sachdev, Magnetotransport in a model of a disordered strange metal, Phys. Rev. X **8**, 021049 (2018).
[123] A. Eberlein, V. Kasper, S. Sachdev, and J. Steinberg, Quantum quench of the Sachdev-Ye-Kitaev model, Phys. Rev. B **96**, 205123 (2017).
[124] R. Bhattacharya, D. P. Jatkar, and N. Sorokhaibam, Quantum quenches and thermalization in SYK models, J. High Energy Phys. 07 (2019) 066.
[125] A. Haldar, P. Haldar, S. Bera, I. Mandal, and S. Banerjee, Quench, thermalization, and residual entropy across a non-fermi liquid to Fermi liquid transition, Phys. Rev. Res. **2**, 013307 (2020).
[126] Y. Cheipesh, A. I. Pavlov, V. Ohanesjan, K. Schalm, and N. V. Gnezdilov, Quantum tunneling dynamics in a

complex-valued Sachdev-Ye-Kitaev model quench-coupled to a cool bath, Phys. Rev. B **104**, 115134 (2021).

[127] J. C. Louw and S. Kehrein, Thermalization of many many-body interacting Sachdev-Ye-Kitaev models, Phys. Rev. B **105**, 075117 (2022).

[128] A. Larzul and M. Schiró, Quenches and (pre)thermalization in a mixed Sachdev-Ye-Kitaev model, Phys. Rev. B **105**, 045105 (2022).

[129] P. Zhang and H. Zhai, Topological Sachdev-Ye-Kitaev model, Phys. Rev. B **97**, 201112(R) (2018).

[130] A. M. García-García, L. Sá, and J. J. M. Verbaarschot, Symmetry classification and universality in non-Hermitian many-body quantum chaos by the Sachdev-Ye-Kitaev model, Phys. Rev. X **12**, 021040 (2022).

[131] S. R. White and A. E. Feiguin, Real-time evolution using the density matrix renormalization group, Phys. Rev. Lett. **93**, 076401 (2004).

[132] U. Schollwöck, The density-matrix renormalization group, Rev. Mod. Phys. **77**, 259 (2005).

[133] M. J. Rice and E. J. Mele, Elementary excitations of a linearly conjugated diatomic polymer, Phys. Rev. Lett. **49**, 1455 (1982).

[134] I. R. Klebanov and G. Tarnopolsky, Uncolored random tensors, melon diagrams, and the Sachdev-Ye-Kitaev models, Phys. Rev. D **95**, 046004 (2017).

[135] E. Witten, An SYK-like model without disorder, J. Phys. A **52**, 474002 (2019).

[136] W.-K. Shih and Q. Niu, Nonadiabatic particle transport in a one-dimensional electron system, Phys. Rev. B **50**, 11902 (1994).

[137] L. Privitera, A. Russomanno, R. Citro, and G. E. Santoro, Nonadiabatic breaking of topological pumping, Phys. Rev. Lett. **120**, 106601 (2018).

[138] See Supplemental Material at http://link.aps.org/supplemental/10.1103/PhysRevResearch.6.013094 for the movies of the time evolution of the spectral and lesser functions as a function of $\bar{t}$.

[139] M. S. Rudner and N. H. Lindner, The Floquet engineer's handbook, arXiv:2003.08252.

[140] J. H. Shirley, Solution of the Schrödinger equation with a Hamiltonian periodic in time, Phys. Rev. **138**, B979 (1965).

[141] H. Sambe, Steady states and quasienergies of a quantum-mechanical system in an oscillating field, Phys. Rev. A **7**, 2203 (1973).

[142] G. Baym and L. P. Kadanoff, *Quantum Statistical Mechanics* (Benjamin, New York, 1962).

[143] J. Rammer and H. Smith, Quantum field-theoretical methods in transport theory of metals, Rev. Mod. Phys. **58**, 323 (1986).

[144] J. Rammer, *Quantum Field Theory of Non-Equilibrium States* (Cambridge University, New York, 2007), p. 536.

[145] A. Kamenev, *Field Theory of Non-Equilibrium Systems* (Cambridge University Press, Cambridge, England, 2011).

[146] A. Picano, J. Li, and M. Eckstein, Quantum Boltzmann equation for strongly correlated electrons, Phys. Rev. B **104**, 085108 (2021).

[147] M. Genske and A. Rosch, Floquet-Boltzmann equation for periodically driven Fermi systems, Phys. Rev. A **92**, 062108 (2015).

[148] A. Stan, N. E. Dahlen, and R. van Leeuwen, Time propagation of the Kadanoff-Baym equations for inhomogeneous systems, J. Chem. Phys. **130**, 224101 (2009).

[149] J. Maldacena and A. Milekhin, SYK wormhole formation in real time, J. High Energy Phys. 04 (2021) 258.

[150] N. V. Gnezdilov, A. I. Pavlov, V. Ohanesjan, Y. Cheipesh, and K. Schalm, Ultrafast dynamics of cold Fermi gas after a local quench, Phys. Rev. A **107**, L031301 (2023).

[151] T. Kitagawa, T. Oka, A. Brataas, L. Fu, and E. Demler, Transport properties of nonequilibrium systems under the application of light: Photoinduced quantum Hall insulators without Landau levels, Phys. Rev. B **84**, 235108 (2011).

[152] P. M. Chaikin and T. C. Lubensky, *Principles of Condensed Matter Physics* (Cambridge University, New York, 1995).